Vortical Patterns behind a Tapered Cylinder

by

Alexandra Hughes Techet

B.S.E., Mechanical and Aerospace Engineering, Princeton University (1995)

Submitted in partial fulfillment of the
requirements for the degree of

MASTER OF SCIENCE IN OCEANOGRAPHIC ENGINEERING

at the

MASSACHUSETTS INSTITUTE OF TECHNOLOGY

and the

WOODS HOLE OCEANOGRAPHIC INSTITUTION

June 1998

Author .....
Joint Program in Applied Ocean Science and Engineering
Massachusetts Institute of Technology
Woods Hole Oceanographic Institution
January 12, 1998

Certified by.... .....
Michael S. Triantafyllou
Professor, MIT
Thesis Supervisor

Accepted by .....
Michael S. Triantafyllou
Chairman, Joint Committee for Applied Ocean Science and Engineering
Massachusetts Institute of Technology and Woods Hole Oceanographic Institution

Vortical Patterns behind a Tapered Cylinder

by

Alexandra Hughes Techet

Submitted to the
Massachusetts Institute of Technology and Woods Hole Oceanographic Institution
Joint Program in Applied Ocean Science and Engineering
on January 12, 1998, in partial fulfillment of the requirements for the degree of
Master of Science in Oceanographic Engineering

Abstract

Visualization studies of the flow behind an oscillating tapered cylinder are performed at Reynolds numbers from 400 to 1,500. The cylinder has taper ratio 40:1 and is moving at constant forward speed U while forced to oscillate harmonically in the transverse direction. It is shown that within the lock–in region and above a threshold amplitude, no cells form and, instead, a single frequency of response dominates the entire span. Within certain frequency ranges a single mode dominates in the wake, consisting of shedding along the entire span of either two vortices per cycle ('2S' mode), or four vortices per cycle ('2P' mode); but within specific parametric ranges a *hybrid mode* is observed, consisting of: a '2S' pattern along the part of the span with the larger diameter; and a '2P' pattern along the part of the span with the smaller diameter. A distinct vortex split connects the two patterns which are phase–locked and have the same frequency. The hybrid mode is periodic, unlike vortex dislocations, and the location of the vortex split remains stable and repeatable, within one to two diameters, depending on the amplitude and frequency of oscillation and the Reynolds number.

To complement visualization results, forces are measured at both ends of a rigid tapered cylinder with span 60 *cm*, performing transverse oscillations within an oncoming stream of water, at Reynolds number $Re \approx 3,800$. Forced harmonic motions and free vibrations of a tapered cylinder are studied. A novel force-feedback control system is used to study free motions. Calculation of the cross-correlation coefficient between the forces at the two ends of the tapered cylinder, in free vibrations, reveals that a regime of low correlation, containing the Strouhal frequency, stretches to higher reduced velocities, while lock-in starts at lower reduced velocities. When comparing free and forced vibration data, we obtain close agreement for the amplitude and phase of the lift coefficient measured, however, the cross-correlation coefficient is higher in the forced oscillations. Hence, although the force magnitude and phase may be replicated well in forced vibrations, the correlation data suggests that differences exist between free and forced vibration cases.

Thesis Supervisor: Michael S. Triantafyllou; Professor, MIT

Acknowledgments

Financial support for this project has been provided by the Office of Naval Research (Ocean Engineering Division), under contract N00014-95-1-0106, monitored by Dr. T.F. Swean Jr. In addition, for the duration of my study, I was supported by the Department of Defense National Defense Science and Engineering Graduate Fellowship Program. This opportunity has allowed great flexibility in my academic pursuits, for this I am grateful.

I would like especially to thank my advisor, Professor Michael S. Triantafyllou, for his guidance and supervision throughout, and Dr. Franz Hover for his assistance and collaboration. Also, my appreciation goes out to the MIT Towing Tank students, especially Ryan Cleary and Bill Kreamer, who helped keep the VCTA experiments running.

Finally, I would like to thank my friends and family who have been supportive throughout. Most of all, my love goes out to my family, mom, dad and Andrew, thank you for all your help and guidance, without which I would not be where I am today.

Contents

List of Figures

Chapter 1

Introduction

1.1 Motivation

The history of vortex induced vibrations (VIV) dates back to ancient times, when it was first noted that as wind would pass over the strings of an Aeolian harp, the strings would begin to vibrate and emit melodic tones.

These vibrations stem from a basic mechanism of fluid dynamics. As fluid passes over a bluff body the pressure forces change. The pressure gradient near a bluff trailing edge of a body is such that the boundary layer separates from the object surface. As this shear layer trails aft of the body, the inner particles of the fluid layer are moving slower than the outer particles causing the shear layer to roll up and form discrete vortices. These vortices are shed from a body, such as a cylinder, periodically from one side then the other forming the well-known Kármán vortex street shown in figure 1-1. In his classical studies in 1912, Theodore von Kármán (1881-1963) investigated wake stability and the relationship between the drag on a bluff body and the structure of the vortex street in its wake. Von Kármán viewed such wake oscillation and the alternate shedding of vortices as an intrinsic flow phenomenon. Today it is known that behind bluff bodies periodicity occurs in some form at all Reynolds numbers from 46 to 10^{11} and perhaps beyond.

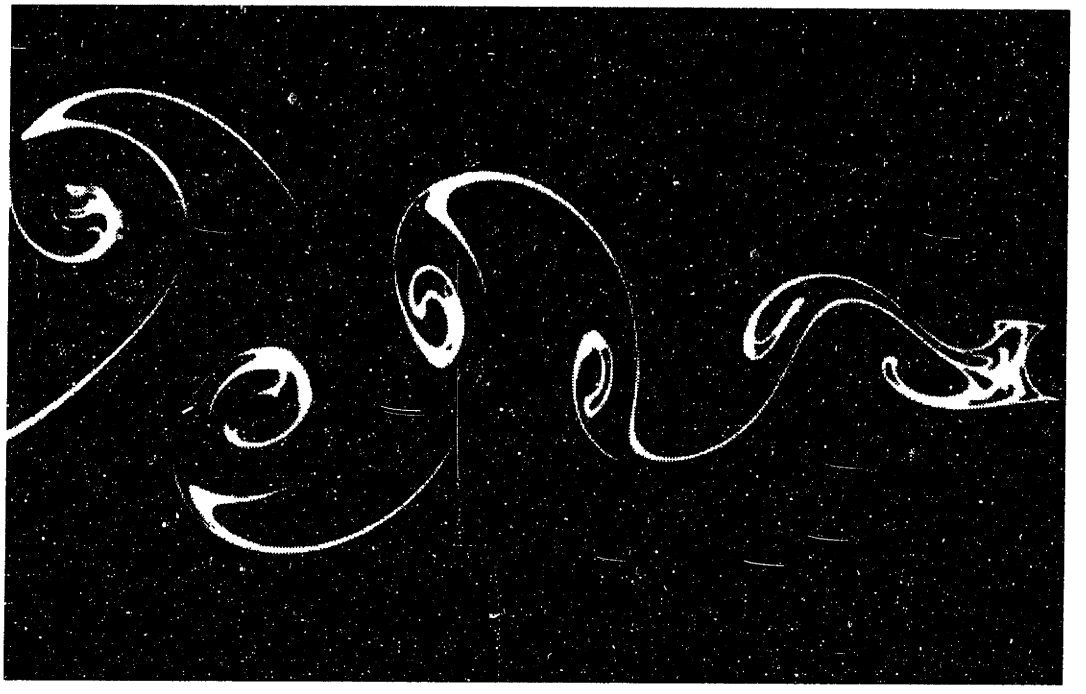

Figure 1-1: The Kármán vortex street in its purest form behind a circular cylinder at $R_d = 140$. Photograph by S. Taneda, from Van Dyke (1982).

The periodic shedding of vortices imposes an oscillating pressure force on the body which can lead to vibrations. If ignored, these so-called vortex induced vibrations can prove catastrophic to structures. While not the only reason for the catastrophes, these vibrations payed a role in the demise of the Tacoma Narrows Bridge in 1940 as well as the popping of windows from the John Hancock Tower in Boston in the 1960's.

The interaction of a slender cylindrical body with a steady cross-flow has been the topic of a great amount of attention, because of the complexity of the viscous flow problem, particularly when interacting dynamically with a structure. The problem is significant both as a paradigm for studying bluff body–flow interaction, and as a practical issue. Engineering applications are widespread and include the aeolian vibrations of tree branches and overhead power lines, marine risers and tension leg platforms (see figure 1-2), and cables strumming within a current. For a wide range of physical parameters, vortex-induced vibrations lead to spatially extended motions of the structure which often result in large dynamic stresses.

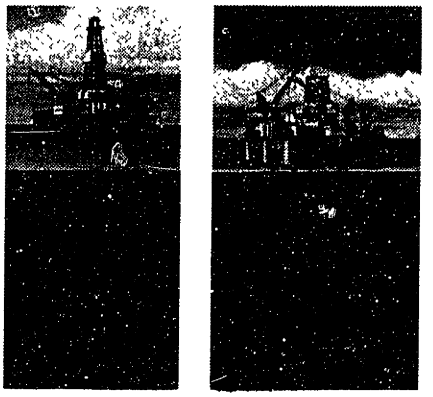

Figure 1-2: Tension leg platform and Marine risers can be adversely effected by vortex induced vibrations

1.2 Vortex Induced Vibrations

1.2.1 Lock-In

Several concepts require definition before proceeding with a discussion on vortex induced vibrations. Since periodic vortex shedding induces an oscillating force on a structure it is necessary to compare the frequency at which vortices are shed, f_s, with the natural frequency of the structure, f_n. When a structure is vibrating at the same frequency as vortices are being shed it is said to be locked on, or in a state of *lock-in.* This is a condition that is of great interest to scientists and engineers since a freely vibrating cable will often *lock-in.*

Along with this idea, it is useful to define a non-dimensional frequency, or a Strouhal number, by which to describe the vortex shedding. Named after Vincez Strouhal (1850-1922), who made some of the first recorded investigations into vortex shedding in 1878, the Strouhal number is defined as

$$S_t = \frac{fd}{U}. \tag{1.1}$$

This number is useful in the study of any bluff body where f is replaced by the frequency of vortex shedding, d the length scale of the body (in the case of a cylinder

d is the diameter), and U the free stream velocity. For a non-oscillating body the Strouhal number remains nearly constant ($S_t = 0.2$) up to $Re = 10,000$.

When parameterizing the flow about oscillating cylinder it is often better to use a reduced frequency, $f^* = fd/U$, or reduced velocity, $V_r = U/fd$, where f is the forcing (oscillation) frequency. This distinction is necessary since the shedding frequency and oscillation frequency are not always equivalent.

1.2.2 Correlation Length

Along the length of a cylinder in non-uniform flow, vortices are shed at different frequencies and are not spanwise coherent. The length over which the shedding is synchronized determines the correlation length. This quantity can yield insight into the spanwise variations in the forces along the cylinder and is often used to initialized numerical codes. Correlation length is expressed in multiples of the cylinder diameter and is determined statistically by comparing the shedding frequency at two points along the cylinder. The length of correlation can vary along the span.

Results from experiments with rigid cylinders show that the correlation increases with heave amplitude.[1] In the case of long flexible cables in uniform flow it has been observed that the correlation length is equivalent to distance between two adjacent nodes of vibration [37]. This observation justifies the use of rigid cylinder sections to model a cable using a strip theory approach [48].

1.2.3 VIV Prediction in Non-uniform Configurations

The prediction of VIV is currently based on semi–empirical methods, often employing a "strip theory" approach and relying on experimental data bases, which are obtained through a number of simplifying assumptions (Blevins [6], Naudascher & Rockwell [32]). Major outstanding problems include the correlation length effects, par-

[1] Heave corresponds to the oscillation of a cylinder transversely to the incident flow.

ticularly in non–uniform cylinders and sheared oncoming flows, and the effect of multi-frequency response. Parallel experimental and numerical efforts are underway to provide better understanding of the phenomenon and develop reliable methods of prediction. Coutanceau & Defaye [10] and Williamson [54] provide recent reviews of progress made in understanding the basic mechanisms of flow response.

While the studies of uniform cylinders and cables in uniform flow are necessary to understanding the underlying phenomenon of vortex shedding, a closer look at more realistic flow configurations is warranted. For instance, the presence of shear flow or non-uniformities in body dimensions introduce initial three-dimensionalities into the flow. Such configurations are of interest in ocean applications, especially since flows in the oceans are rarely uniform. Wind and currents often produce sheared flow which can adversely affect marine structures.

The basic case of linear shear flow about a uniform cylinder has revealed that vortices are shed in "cells" of different frequencies. discontinuities in frequency exist between each cell [42] and lead to complex vortex reconnection and the emergence of longitudinal vortices. An analogous problem is that of a linearly tapered cylinder in uniform flow. Similar results to shear problem have been obtained for this configuration. Anderson and Szewczyk [3] showed that a tapered cylinder in the reciprocal sheared flow (the larger end of the cylinder aligned with slower portion of the shear flow) yielded results analogous to a uniform cylinder in uniform flow.

Further discussions of tapered cylinders will be made in Chapters 3 and 4.

1.3 Chapter Preview

Chapter 2 reviews several flow visualization and measurement techniques and discusses those used throughout this study. It details both a qualitative and quantitative method of flow observation. The lead precipitation method is presented as a purely qualitative technique, and Digital Image Particle Velocimetry (DPIV) as a

quantitative instantaneous measurement of the velocity field in two dimensions.

Three-dimensional and small scale features observed in the tapered cylinder wake are presented in Chapter 3. The difference between the laminar cases and turbulent cases is clearly shown with the presence of shear layer vortices at $R_{\overline{d}} = 1500$. The difficulty in pin-pointing a correlation length is understood due to the presence of rib vortices which act to deform the main vortex line. The influence of various end conditions and how they effect the spanwise shedding will be discussed briefly. The non-oscillating case of the 40:1 tapered cylinder is presented in this section as well.

Chapter 4 introduces the effects of forced oscillations on the tapered cylinder. Shedding patterns determined by Williamson and Roshko [55] are discussed in relation to the case of the tapered cylinder. In theory it can be predicted that one shedding pattern might exist along the length of a sufficiently tapered cylinder. Evidence supporting this is presented and suggestions are made on how two different vortical patterns might connect.

Chapter 5 ties in a series of force measurements done on both the freely vibrating and forced-oscillating tapered cylinder. Free motions are studied using a force-feedback control system developed at the MIT Towing Tank. Lift forces at each end of the cylinder are measured and the correlation coefficient is calculated between the two forces. This correlation is used to gain insight into the spanwise variation in the forces on the cylinder.

Chapter 2

Experimental Methods

The experimental study of fluid flow has a rich history dating back to the 15th century when sketches by Leonardo da Vinci revealed flow features such as water waves, eddies, floating bodies, flow in pipes and channels, and flow around objects. He was one of the first to suggest using particles floating in the water to observe flow. Since ancient times the experimental study of fluids has grown into a leading scientific interest. This interest has opened the door to a wide array of flow measurement and visualization techniques.

Early studies of flow were done using various dye tracers to observe the various flow structures. Such techniques are invaluable in many cases of laminar flow and even when observing the larger scale features of some turbulent flows. However due to the speed at which most dyes diffuse, it is difficult to catch the finer scales present in higher Reynolds number flows.

More recently, techniques have evolved to visualize the smaller scale features present in turbulent flows. Such observations require a finer resolution. Therefore various point measurement techniques and particle imaging methods have evolved. The advent of lasers has proved extremely useful in such studies [1, 2].

Initial attempts at flow field mapping were done using time intensive techniques such as Laser Doppler anemometry (LDA) and Laser Doppler Velocimetry (LDV).

These non-invasive point measurements yield good temporal resolution, however better spatial resolution is warranted. Unlike other particle methods, DPIV allows the measurement of an entire instantaneous two-dimensional velocity field and the corresponding vorticity.

2.1 Flow Visualization

Visualization experiments were performed at the MIT Testing Tank Facility. A tapered test section was towed at steady forward speed while oscillating in the transverse direction, and the vortical patterns and fluid forces were recorded. First, an electrolytic precipitation method provided insight on the qualitative behavior of the wake as function of the amplitude and frequency of oscillation. Then, digital particle image velocimetry (DPIV) provided quantitative data of the instantaneous velocity field and its associated vorticity along a plane of interrogation.

2.1.1 Flow-Visualization Set-Up

The flow–visualization experiments were conducted in a glass tank with dimensions $2.4m \times 0.75m \times 0.75m$. A motor-driven carriage moves along the top of the tank at constant speed, up to 20 cm/s, driven by an AC motor. An oscillating mechanism is mounted on top of the carriage, which imposes forced harmonic oscillation with amplitudes up to 7.62 cm; the frequency can be varied continuously from 0 to 0.7 Hz. The layout of the apparatus is shown in Figure 2-1. The force measurement experiments were performed in the adjacent testing tank which is $30.5m$ in length, $2.5m$ wide and on average $1.5m$ deep.

The tapered cylinder was a wooden spar coated in a layer of lightweight fiberglass cloth. Epoxy was applied twice to increase the stiffness and avoid swelling due to water absorption. The cylinder dimensions are $d_{max} = 3.2$ cm, $d_{min} = 1.55$ cm, the average diameter, $\overline{d}$, is 2.4 cm, and the overall length of taper, l, is 66 cm. The taper

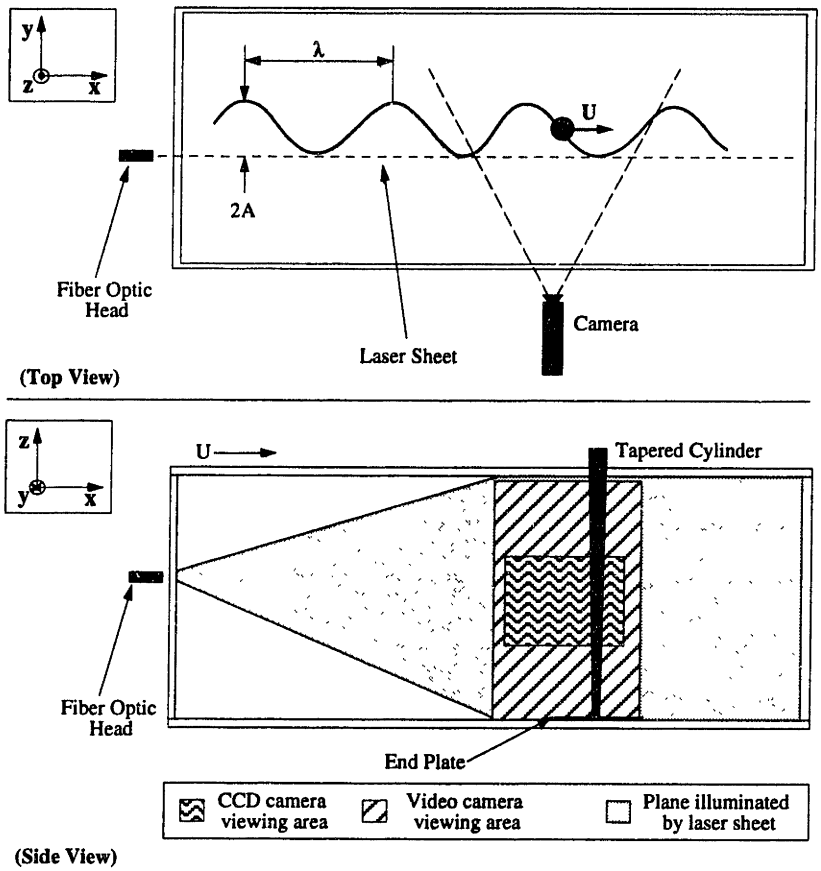

Figure 2-1: Experimental Setup: Top and Side Views

ratio is defined by:

$$\tau = \left| \frac{l}{d_{max} - d_{min}} \right| \tag{2.1}$$

Using equation 2.1, the taper ratio is equal to 40:1. The cylinder reaches very close to the bottom of the tank, 72 cm deep, but the taper only extends from the bottom up to 66 cm. The cylinder was not fitted with end plates in order to facilitate visualization; the gap between the lower end of the cylinder and the bottom was less than 0.5 *cm*, which was found to reduce end effects to within two diameters from the lower end, in agreement with the findings by Slaouti & Gerrard [41].

Both visualization methods employ a high resolution, black and white CCD video camera, Texas Instruments MULTICAM MC1134P, which recorded the flow with a

maximum pixel resolution of 1134 x 480 pixels at a standard frame rate of 30 Hz. Dual field exposure rendered full vertical resolution with no interlace. The video from the CCD camera is stored real-time directly to a Sony CRVdisc video–disc recorder (LVR-5000A). The video frames are digitized at 8 bits/pixel by an EPIX 4MEG video board in a 486 PC. In the lead precipitation method, a standard video camera is also employed to observe the shedding patterns along the entire length of the cylinder.

A mechanical shutter was used in the DPIV experiments to reduce the exposure time of the images, thus changing the effective framing rate of the camera from 30 Hz to 15 Hz. This triggering allows the images to be grouped into pairs separated by 1.5 milliseconds. A General Pixels Timing box synchronized to the video signal controls the laser shutter.

The seed particles in both methods are illuminated by light from a 6 watt continuous beam Argon-Ion laser. The light from the laser passes through the mechanical shutter and into a fiber optic cable which extends to the experimental area. At the far end of the cable, the head of the fiber optic cable spreads the laser beam into a sheet in order to illuminate an entire 2D plane in the flow field. For the visualizations of the vertical planes, the laser sheet is positioned at the point of maximum oscillation and captured by the camera through the side window of the tank. For the horizontal slices, the laser sheet is placed at the location along the span which is of interest and the camera records the image through a window in the bottom of the tank.

2.1.2 Lead Precipitation

Lead precipitation is used to obtain a qualitative understanding of the shedding patterns in the cylinder wake, and is a variation of the electrolytic precipitation method outlined in a paper by Honji, Taneda, and Tatsuno [22]. Their method involved the coating of a test section with a tin solder, whereas our method employs a thin lead foil strip that is introduced along the stagnation line of the cylinder. This lead precipitation method is similar to that outlined in Anderson and Szewczyk [3].

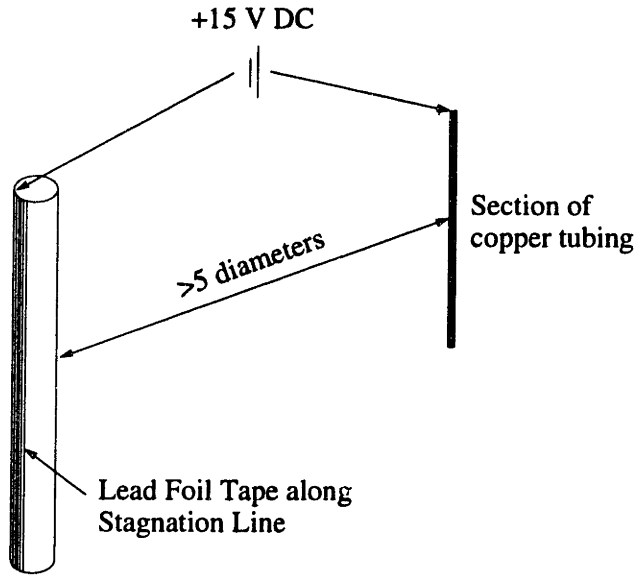

Figure 2-2: Lead Precipitation Configuration

Lead precipitation is achieved by placing a strip of thin lead foil tape along the stagnation line of the cylinder and connecting it to one pole of a DC power supply. The other pole may be connected to a conducting plate, or as in the present experiments, to a section of copper tubing which serves as the cathode (see figure 2-2). This copper tubing is placed sufficiently downstream and the side of the cylinder such that it does not affect the vortex formation process and does not obstruct the area of flow being observed.

When a voltage differential is applied across the two poles, a cloud of lead particles precipitates into the flow. The foil tape can be molded into any shape, thus allowing it to be smoothed into the leading edge of the cylinder and providing a non-intrusive method of flow visualization. The particles are emitted from the leading edge directly into the boundary layer of the cylinder. This makes the lead precipitation method very useful for observing the separation of the shear layer.

The flow visualization tank is filled from a distilled water source which is not conductive. Thus in order for lead precipitation to be successful an additive must be introduced to enhance the water's conductivity. This additive can be simple table

salt; the quantity of salt is not so critical.

The lead precipitate is illuminated by the 6 Watt Argon-Ion laser, operating at less than half power, which was found to be adequate for these experiments. Suggestions for improvement on the present configuration include the use of a copper tape, instead of tubing, placed on the cylinder parallel with the lead strip.

The images recorded by the second, standard video camera were used to record the different spanwise shedding patterns and also to determine the point at which dislocations occurred. The resolution of the second camera was not always sufficient to capture certain details. The images obtained from the CCD camera yielded the needed detail, but only captured a portion of the spanwise the shedding between $z/\overline{d}$ = 9.75 and 14.75. The total height of the images obtained with the CCD camera is five average diameters.

2.1.3 DPIV Method

Quantitative velocity field measuring experiments were conducted using Particle Image Velocimetry [1] as implemented digitally by Willert and Gharib [51]. A plane is illuminated using a laser beam fanned to form a plane sheet; and the fluid is seeded with neutrally buoyant fluorescent particles (diameter $\approx$ 40 to 70 μm) which reflect wavelengths in the range of 560-580 nm. Willert and Gharib [51] found that 10 to 20 particles per interrogation window were sufficient to ensure good correlations. Camera positioning must ensure that the particle images are approximately 2-3 pixels in size, since the algorithm cannot resolve sub-pixel images.

Image data from two successive video frames are collected and stored digitally in levels of grayscale. In each of the frames we examine small interrogation windows at the same spatial position and the data, $f(m,n)$ and $g(m,n)$ are used to calculate the

cross-correlation function,

$$\Phi_{fg} = f(m,n) \circ g(m,n) = \sum_{k=-N/2}^{N/2-1} \sum_{l=-N/2}^{N/2-1} f(k,l)g(k+m,l+n) \qquad (2.2)$$

where m, n refer to the individual pixels and N is the size of the interrogation window in pixels (see Figure 2-3). This cross-correlation measures how closely the two images match.

A strong narrow peak in the correlation function provides the average displacement of the sampled group of particles. The correlation peak is located with sub–pixel accuracy using a Gaussian curve fit to the data around the maximum correlation value in both image directions independently. The Gaussian fit take the form

$$p(\zeta) = c_1 e^{\frac{-(\zeta - c_2)^2}{c_3}}. \qquad (2.3)$$

The correlation maximum and four additional data points, as indicated in Figure 2-3 by the encircled points in the peak finder box, are used to complete the model. This model works best when the peak is broad and particle images are larger than a few pixels in size.

The effect of the DPIV windowing process is that of a spatial low-pass filter. Using the analysis in Willert and Gharib [51], we observe a 40% attenuation of features on the order of 64 pixels when a 32 × 32 window is used in the processing. The attenuation is limited to less than 10% for features nearing 160 pixels in size. Similarly, for a 16 × 16 processing window, features on the order of 32 pixels are attenuated by approximately 35%, and a 10% attenuation is realized for features near 75 pixels in size. We estimate a mean relative RMS error of 5–6% for particle displacements in the range of 0 to 9 pixels; absolute errors ranged from 0.01 pixels to 0.15 pixels. Increased seeding densities beyond 20 particles per 32 × 32 window show no significant improvement in uncertainty. A typical relative RMS error for moderate pixel

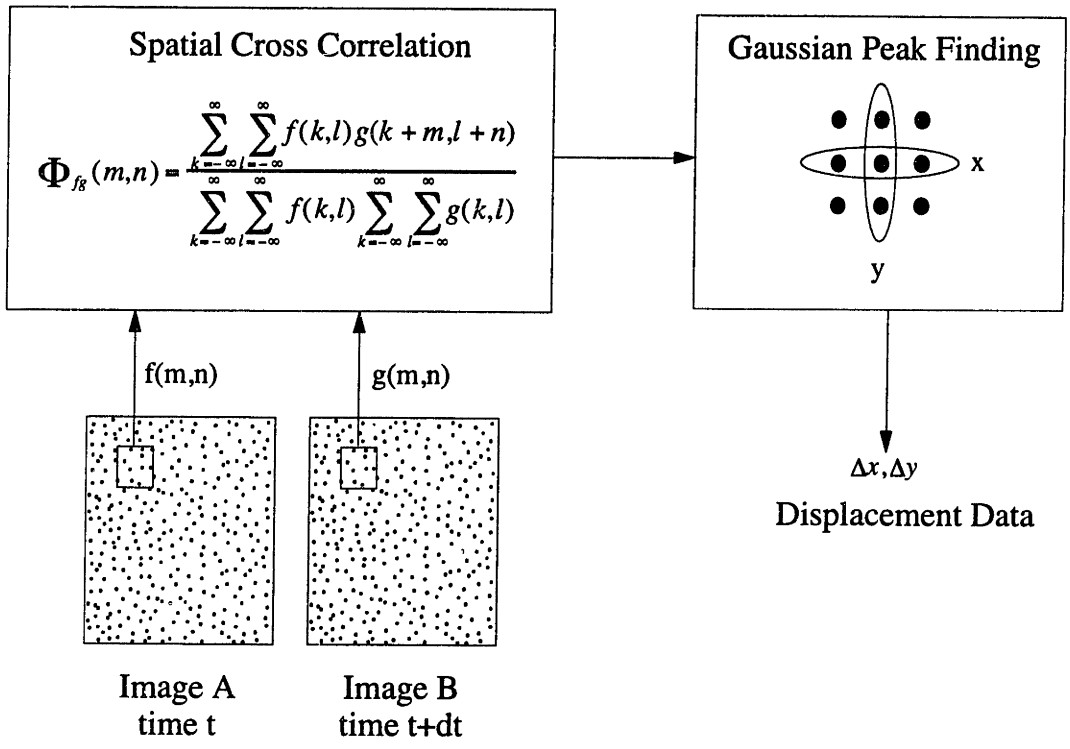

Figure 2-3: DPIV Algorithm

excursions (greater than 1 pixel) is of the order of 5%. In terms of velocity this results in typical absolute error of 0.2 cm/s for a time step of 20 ms, resulting in a relative velocity error of 7.5%.

2.2 Force Measurements

Force measurements are a valuable method of determining the effect of a fluid on an object. The connection between force measurements and flow visualizations can be used to create a more complete picture of the flow field and its effect on an object within.

Traditional force measurements have been done using techniques such as hot wire anemometry, pressure transducers or load cells attached to an object in the flow. Each method has its advantages and disadvantages. For the problem treated in this

study, force transducers present the ideal method for studying the end forces acting on the cylinder.

2.2.1 Force Measurement Set-up

The force measurement experiments were conducted at the MIT Testing Tank Facility in the main still-water tank with dimensions $30m \times 2.5m \times 2.5m$. The tank is equipped with a double-rail structure supporting a motor driven carriage, which can operate at speeds between 0.1 to 1.5 m/s. The carriage setup outlined in Figure 2-4 was first created by [16] and more recently modified as described in [23] and [24]. The cylinder test section is 62 cm long with the same taper ratio used in the visualization experiments. The average diameter of the cylinder is 2.78 cm and the cylinder fits into the apparatus with the small or large end of the cylinder at either end of the load cell. The test section is supported, in an inverted U-frame yolk assembly, by a Kistler load cell at either end.

The yolk is connected to a linear lead screw table, driven by a Parker-Hannifin servomotor and MEI motor controller card, which are used to oscillate the yoke up to an amplitude of 8 cm. The trajectories of the servomotor are mapped out by an on-board 486 computer, in both the case of the forced oscillation and the "freely" oscillating cylinder. The forces measured at the ends of the cylinder are comprised of inertial forces from the test section at its fittings as well as the hydrodynamic forces that arise from the cylinder motion through the water.

The compliant system is simulated on-line as dictated by the following force model: $m\ddot{x} + b\dot{x} + cx = F_{hydrodynamic}$. The inertial component of the measured force must be subtracted from the force signal in order to obtain the hydrodynamic force in real-time. Now, working with only the hydrodynamic force, a wide range of damping and stiffness coefficients can be used with the same test section. The 40:1 tapered cylinder has a specific mass of 1.33, a virtual specific mass is defined as $m^* = 4m/\pi d^2 l$.

Examining the model used in the compliant system it can be noted that the

damping term could be set to zero. This is not feasible in practice as the servomotor and feedback loop carries no assurances that there will be a zero net power flow when the damping term is zero, thus any small error in timing could drive the system unstable. Test were previously done with the apparatus in air and the lowest damping ratio measured was approximately 0.013. This is the value then expected as the minimum mass-damping parameter, $m^*\zeta$.

The end forces are measured with two Kistler piezoelectric transducers placed just inside of the vertical struts supporting the ends of the tapered cylinder. Two identical end plates are attached to the vertical struts, but in no way alter the motion of the cylinder or affect the forces measured by the Kistlers. The end plates are parallel to the direction of flow and are approximately ten times the average diameter of the cylinder. The tests performed with this apparatus are at Reynolds number 3,800, thus the forces measured are not large. The resolution of the force sensors is sufficient, 0.005 Newtons. The force-feedback system requires real-time filtering of the signal which is accomplished using a Butterworth low-pass filter, with a cut-off of 22 Hertz. A digital filter is used to apply the same phase to the inertial correction for consistency.

The imposed motions are measured using a Schaevitz Linear Variable Differential Transformer (LVDT) HR 3000 with a linear range of $\pm 8cm$. The Kistlers and LVDT are operated through amplifiers located on the carriage, close to the sensors. The signal outputs are sent both to the simulation computer and the data acquisition board which is located in a second computer located away from the carriage.

Data processing is completed to obtain the quantities discussed next. The records are broken up into packets of two oscillations and a mean and RMS value of the signals are retrieved. High RMS values imply fluctuations over the duration of the run whereas low RMS values imply stable qualities. The parameters derived from the data collected are:

- Nominal Reduced Velocity, $V_{rn} = U/df_n$, where f_n is the structural vibration frequency.
- True Reduced Velocity, $V_r = U/df_o$, where f_o is the observed frequency of vibration.
- Lift Coefficient in phase with velocity:

$$C_{lv} = \frac{F_l}{\frac{1}{2}\rho dLU^2}, \tag{2.4}$$

  where F_l is the lift force in phase with velocity, calculated using the inertia-corrected force and velocity in an inner product. The diameter used is consistent with the local diameter at each end of the tapered cylinder.
- Lift coefficient in phase with acceleration, C_{la}, defined using the (inertia corrected) force in phase with acceleration. Added mass is positive when C_{la} is negative.
- Phase, ϕ, by which the force leads the position.
- Cross-correlation, F_c between the two end force signals. The sample standard deviation of this correlation is defined as μ. A correlation coefficient near one suggests uniform flow across the cylinder span.

Forced and "Free" oscillation tests were performed in duplicate and triplicate.

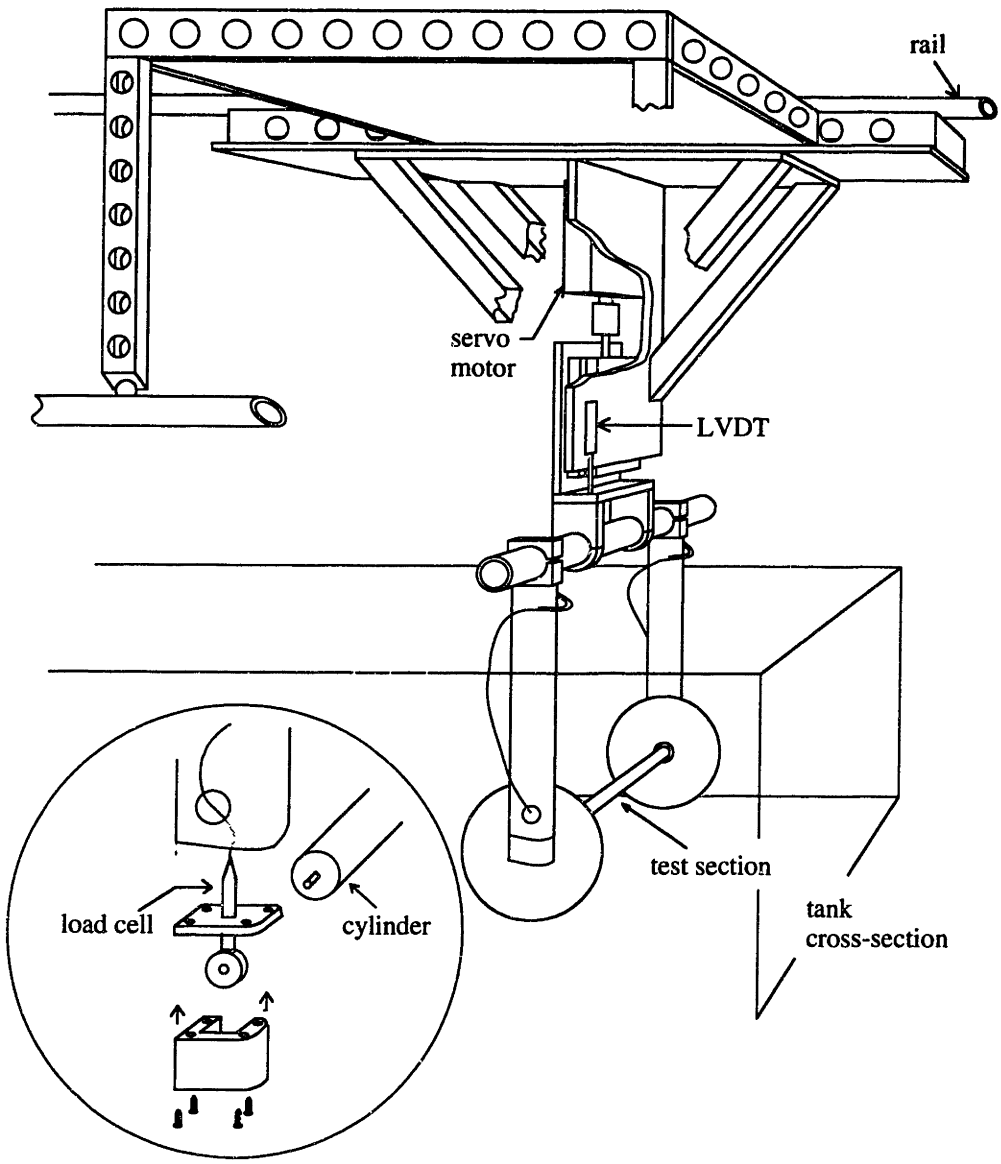

Figure 2-4: Test section and carriage schematic

Chapter 3

Secondary Vortical Structures

Roshko [38] identified the transition to irregular vortex shedding to be in the range of Reynolds numbers between 150 and 300. Recently, investigation of three–dimensional patterns in nominal two–dimensional flows has shed much light on the physical mechanisms, particularly at low Reynolds numbers. Coutanceau & Defaye [10] have provided a detailed overview of the shedding process for stationary and moving cylinders, covering a very extensive literature. Williamson [53] reviews the cascade of phenomena appearing as Reynolds number is increased from the stable laminar range $Re < 49$, to supercritical values $Re > 10^6$. The three–dimensional transition of the wake starts at $Re \approx 190$ with the formation of modes A and B in Williamson's nomenclature; Mode B dominates after $Re \approx 250$ and results in the formation of longitudinally directed fine scale vortices with a typical distance one diameter from each other. These rib–like structures connect and wrap around the Karman vortices; they have been studied by Wei & Smith [50], Bays-Muchmore & Ahmed [4], Wu et al. [57, 56], Szepessy [44], Towfighi & Rockwell [46], Chyu & Rockwell [9], at higher Reynolds numbers by Lin et al. [30], and Zhou & Antonia [60], among others. The streamwise vortices scale with the Karman vortices even when secondary shear layer (Bloor) vortices are present. Triantafyllou [47] considered theoretically the problem of three–dimensional patterns in a nominally two–dimensional wake; Karni-

adakis & Triantafyllou [26] studied the same problem numerically, finding the wake inherently three–dimensional for $Re > 200$.

3.1 Cellular Vortex Shedding

As discussed in chapter one, vortices are thought to shed in "cells" along the length of a cylinder in non-uniform flow or in the presence of end effects (see figure 3-1). Within each cell the vortices form at the same frequency, however from one cell to the next the shedding frequency can vary.

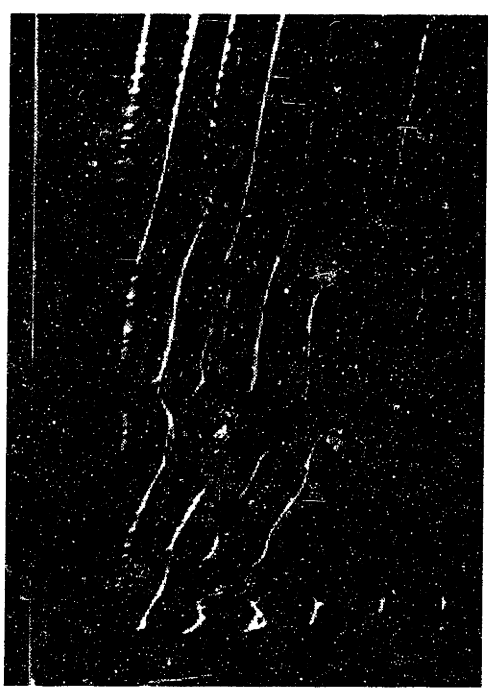

Figure 3-1: Here cells of different frequency are shown for a cylindrical section stationary to an incident flow. From Konig et. al [28].

Piccirillo and van Atta [36] show that vortex splits form the link between shedding cells (one vortex would break into two at a cell boundary). It is noted that cell size increases with local diameter, and that the frequency associated with each cell is determined by the average local diameter of the cylinder and a local average Strouhal

number [14].[1] Piccirillo and Van Atta then assume that if the cylinder geometry is governing the flow then the cells scale by a "self–similarity hypothesis" which finds that cells are proportional to local diameter at each cell midpoint.

Also, as the Reynolds number increases, the cell size was found to converge to a constant value. Taper produces a geometric effect in determining number of cells along cylinder and less taper ratio shows more regular shedding and splitting patterns. For the smallest taper vortices are initially shed nearly parallel, in a continuous vortex line which tends to bend over. As these lines steepen a vortex split occurs nearest to the small diameter end first. Splits occur in succession moving from the small-diameter to the larger-diameter end. After the last split the vortex line is nearly parallel and continuous.

Williamson [52] illustrates how vortex dislocations are largely responsible for breakup to turbulence of the wake. One-sided dislocations are generated between spanwise cells of different frequency–when von Kármán streets are out of phase. In laminar vortex shedding regime, dislocations occur between cells with different frequencies and associated with certain oblique vortex shedding modes.

3.2 Oblique Shedding

The shedding of vortices behind stationary cylinders may occur at oblique angles depending on end conditions or inhomogeneities. Oblique shedding affects the frequency of shedding and onset of transition (Ramberg [37], Hammache & Gharib [21], Williamson [53]). There is close connection between oblique shedding and end effects or discontinuities in the cylinder properties, resulting in the formation of cells of different inclination and frequency of shedding (Konig et al. [28], Lewis & Gharib [29], Yang et al. [58]). Cylinder oscillation alters the angle of oblique shedding, while proper end conditions can be imposed to ensure parallel shedding. These phenomena

[1] $S_t = 0.2$ based on local diameter.

were seen in this study of the 40:1 tapered non-oscillating cylinder as well.

Gaster [13, 14] studied tapered cylinders as well, with the point of detachment migrating from the smaller to the larger diameter end of the cylinder, forming "y-type" structures in the wake. Numerical studies by Graham and Arkell [18] on a vertical, 40:1 tapered cylinder in waves revealed similar y-type structures to those observed by Gaster. Papangelou [34] found that the vortex angle increased within a cell as it jumped to the next cell and then dropped again.

3.3 Three-dimensional Wake Structures

The idea of three-dimensional structures present in the wake have been presented by researchers such as Bloor [7], Gerrard [15] and more recently by Wu, et al. [56]. Such three-dimensional structures are thought to be the essence of the transition from laminar to turbulent flow [20].

3.3.1 Shear Layer Instability

It is known that, at a certain Reynolds number, the flow in the cylinder wake becomes turbulent. It has also been realized that at some point the shear layer also becomes unstable as it separates from a bluff body. Bloor [7] studied the instability of the shear layers emanating from the cylinder, which results in the formation of secondary vortices. When the primary Kármán vortices are shed parallel to the cylinder axis, the transition Reynolds number at which the secondary instability is first observed, is about 1,200; under oblique shedding conditions the critical Reynolds number varies substantially.

In the present study such shear layer instabilities were noted in several of the lead precipitation visualizations perpendicular to the cylinder axis. At $R_{\overline{d}} = 400$ no such features are noted, however at $R_{\overline{d}} = 1500$ it is quite clearly observed. Figure 3-2 illustrates the two cases.

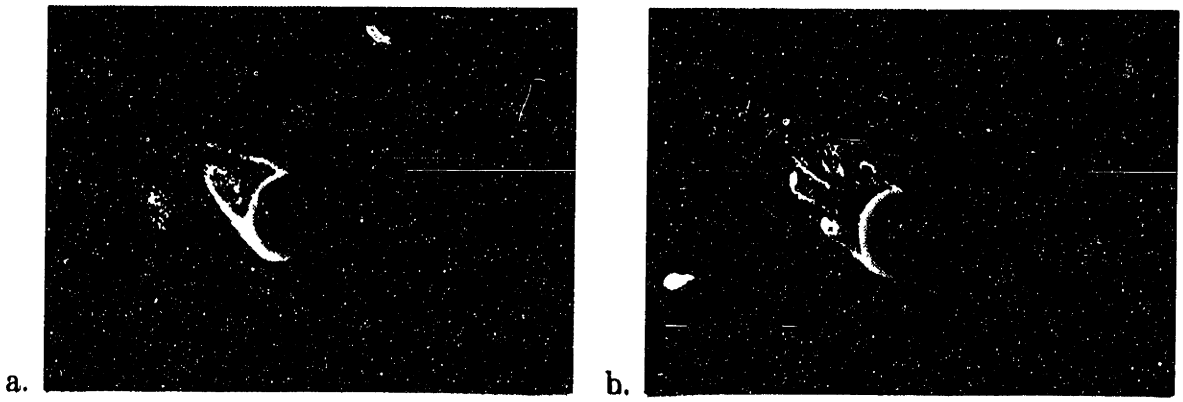

Figure 3-2: Comparison between (a.) $R_{\bar{d}} = 400$ and (b.) $R_{\bar{d}} = 1500$. At $R_{\bar{d}} = 1500$ the appearance of Bloor vortices in the shear layer is apparent.

3.3.2 Streamwise Vortices

Some of the first observations of streamwise vortices were done by Gerard [15] in dye-visualizations of the shedding behind spanwise-uniform cylinders for Reynolds numbers greater than 140. These visualizations revealed the presence of three dimensional structures in the form of "dye-fingers" along the cylinder span. Streamwise vortices are often referred to as rib or longitudinal vortices–for consistency these features will be called streamwise vortices in this paper. More recently, studies by Wu, et al. [56] contribute these fingers to the presence of longitudinal vortices inclined at an angle to the streamwise direction.

Wu, et al. introduce the use of DPIV to observe the streamwise structures in a cylinder wake. They are able to detect these vortices present along the span of a uniform cylinder in uniform flow. Figure 3-3 is a schematic representation of the longitudinal vortices. Note that these secondary vortices are shown to be inclined at an angle to the streamwise direction.

Flow visualizations of these small vortices appear as mushroom–type structures in the near wake.In the case of the 40:1 tapered cylinder streamwise vortices are captured using DPIV. For the non-oscillating tapered cylinderat $R_{\bar{d}} = 800$ ($Uo = 3.4\ cm/s$), figure 3-4 shows the streamwise vortices clearly. Image (a) represents the instanta-

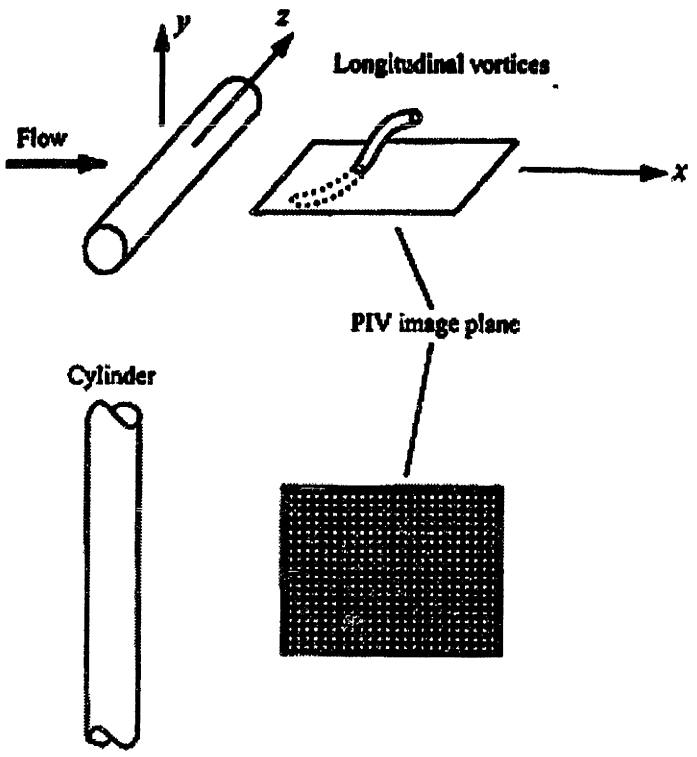

Figure 3-3: Schematic representation of streamwise (longitudinal) vortices inclined at an angle to the incident flow. Taken from Wu, et al. (1996).

neous two–dimensional velocity field in the $(x - z)$–plane, one average radius from the centerline of the cylinder. This DPIV vector field is not extremely informative. However, figure 3-4b shows the streamwise structures in a vector plot of the velocity where the estimated convective speed of the streamwise vortices has been subtracted out(60% of the free stream velocity as suggested by Wu, et al.). Finally the vorticity plot (b) clearly shows the three longitudinal vortices as they intersect the $(x - z)$–plane.

Results from Wu et al. [57] show similar features for a uniform stationary cylinder.[2] The second image, figure 3-5b, is the original velocity field minus an estimated convective speed of the longitudinal vortices (Uc=0.6*Uo). Streamlines shown in figure c again illustrate these features. Velocity section cuts through the center of the

[2]All visualization by Wu, et al. reproduced here are for Reynolds number 525.

longitudinal vortices reveal an oscillating streamwise velocity at the location of the secondary vortices. Which explains why it is difficult to determine a definitive value for correlation length using an instantaneous velocity field. Wu, et al. noted that the longitudinal vortices tended to wander along the span of the cylinder–attempts to lock the vortices were unsuccessful.

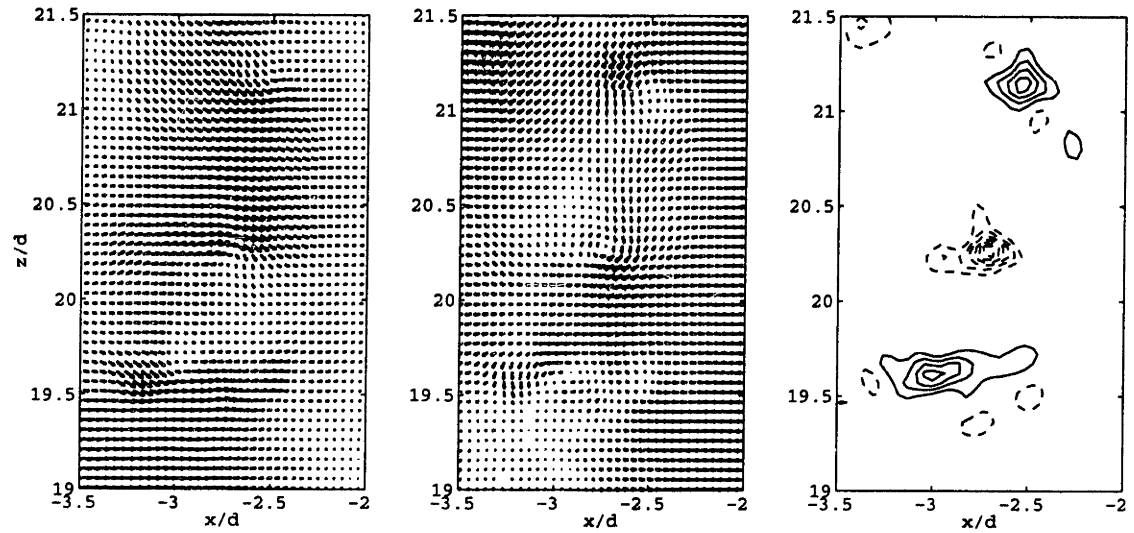

Figure 3-4: DPIV images of the non-oscillating 40:1 tapered cylinder at $R_{\overline{d}} = 800$. Figure (a) shows the two–dimensional velocity field in a stationary reference frame, (b) in a reference frame moving at 60% of the free stream velocity, and (c) the corresponding vorticity plot.

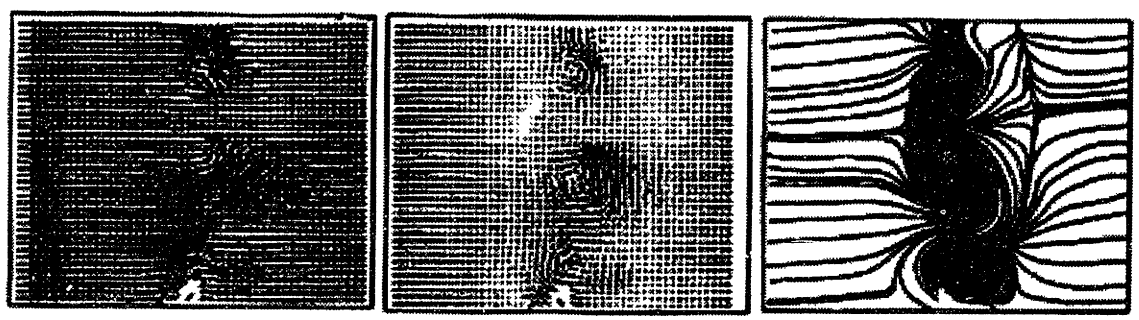

Figure 3-5: DPIV velocity fields at Reynolds number 525: (a) velocity field (stationary reference frame); (b) $U = 0.6 * Uo$ (reference frame moving at convective speed of streamwise vortices); (c) streamlines derived from velocity map. Taken from Wu, et al. (1996).

3.4 End Effects

Vortex shedding behind cylinders has been found to vary greatly depending on the conditions at the ends of the cylinder. While much work has been done to investigate these effects, careful study should be done for each experimental setup. Several different end configurations can be considered:

- Clean free surface
- Contaminated free surface
- End plates
- Free end near wall
- Free end away from wall

Each configurations has its own effect on the vortex shedding pattern in a cylinder wake.

3.4.1 Free-surface Effects

At a water-air interface surface tension can play a role in the evolution of vortices shed from a cylinder that pierces the surface. Contaminated surfaces lead to wake crowding and bowing of the vortices towards the cylinder at the free surface because the vortices must connect under the free surface [41]. If the vortices are formed at a clean water surface, and can "go through" the surface, then the vortices will link in the air above. Contaminated surface is one with patches of film or completely covered with a film (say a surface-active substance such as detergent). A clean surface has no such contamination. Slaouti and Gerrard noted that the presence of a few 'dust' particles that often make their way onto the surface during the course of experimentation, did not alter the water surface condition. They also noted that the presence of a detergent film on the surface did not alter the perpendicular shedding from the case of the clean surface.

a. 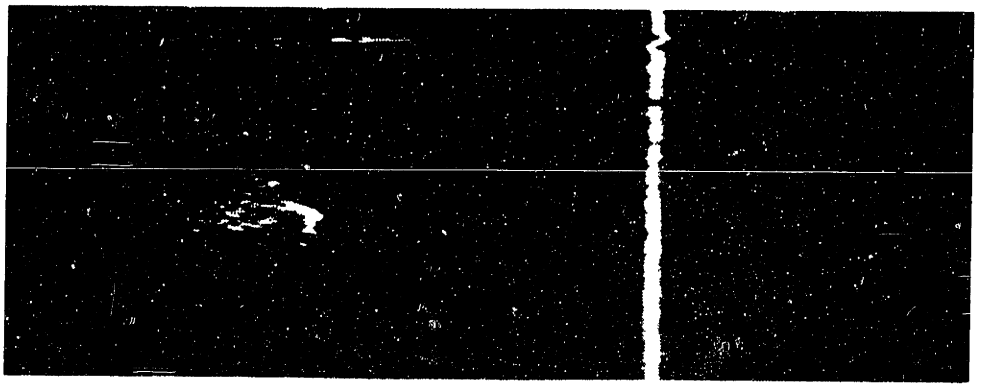

Figure 3-6: Effects at a clean free surface with the 40:1 oscillating tapered cylinder at $R_{\overline{d}} = 1500$, $A/\overline{d} = 0.25$, $S_t = 0.18$. The laser sheet is positioned on the centerline of the cylinder ($y = 0$).

For the experiments performed in this study, a "clean" free surface was obtained using a few drops of liquid detergent to create a thin film on the surface, and then siphoning it off through a stand-pipe at the other end. Thus the result was a clean water surface. As is seen in figure 3-6 this method was successful in obtaining parallel shedding at the free surface. Throughout the course of experimentation this process was repeated due to the continuous recontamination of the surface due to the lead particles being shed exactly at the surface. These particles tended to "stick" to the surface and effect the shedding if not cleared between runs. A contaminated surface will remain stationary after the cylinder has passed through. This results in the bending of the vortex lines under the free surface. The vortices no longer lie perpendicular to the surface and seem to reconnect at the stagnation point on the front of the cylinder [41]

3.4.2 End Plate Effects

Like the contaminated surface, a solid interface will cause the vortex lines to bend away from the boundary thus leading to a complex linking mechanism. This mechanism will be determined by the type of boundary at the end of the cylinder. For

instance if the cylinder is bound by an end plate traveling with the cylinder, then the boundary layer on that end plate will effect how the shed vortices connect. Lead precipitation visualizations performed in the present study (figure 3-7) show vortices being shed perpendicularly to the cylinder. It is also observed that the shed vortices tend to interact and connect with each other as is seen in the left portion of the image. The use of the end plate results in similar shedding patterns in both the case of the

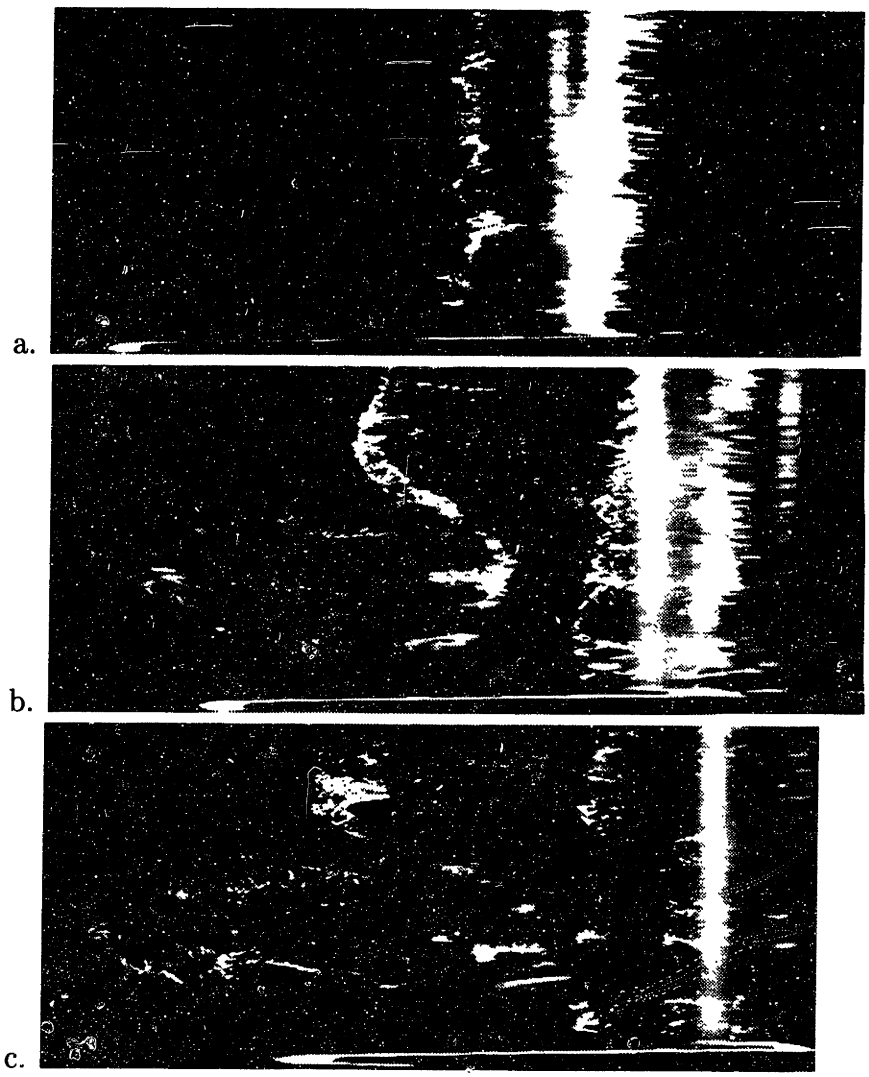

Figure 3-7: End Effects. 40:1 Tapered Oscillating Cylinder with end plate. $R_{\overline{d}} = 1500$, $A/\overline{d} = 0.25$, $S_t = 0.18$.

oscillating (figure 3-7) and non-oscillating (figure 3-8) tapered cylinder.

If the cylinder end is sufficiently far enough away from the wall of a tank and no end plate is attached, then the vortices tend to deflect upwards (away from the free end, up into the wake) behind the body. This configuration tends to have the most severe effect on the vortex shedding and should be avoided [41].

Slaouti and Gerrard also showed that when the cylinder end was placed sufficiently close to the bottom of the tank, vortex shedding remained perpendicular to the cylinder axis and did not bow, as in the case of the free end away from a wall. For the majority of cases studied in this paper, no end plate was used. Yet the lower end of the cylinder was placed in accordance with Slaouti and Gerrard's findings—very close to the tank bottom. Here parallel shedding results as shown in figure 3-9.

3.5 Summary

Williamson and Roshko, and Wu, et al. have identifies basic mechanisms for the flow behind a uniform cylinder. We extend these concepts to cases where non-uniform shedding occurs along the span of the cylinders, thus introducing the connection to the correlation length.

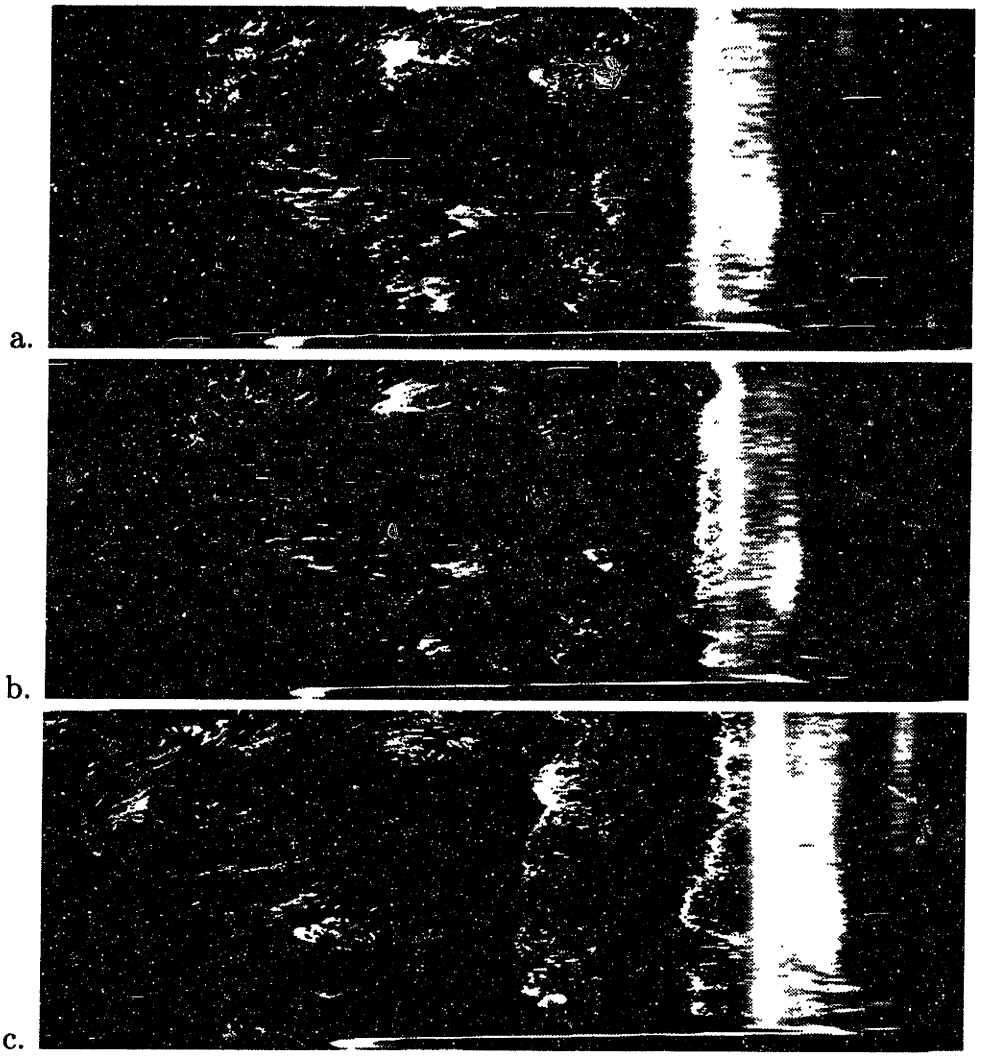

Figure 3-8: End Effects of a 40:1 Tapered NON-Oscillating Cylinder. Endplate diameter is $6 * \overline{d}$. $R_{\overline{d}} = 1500$. Laser sheet at cylinder edge ($y = \overline{d}$).

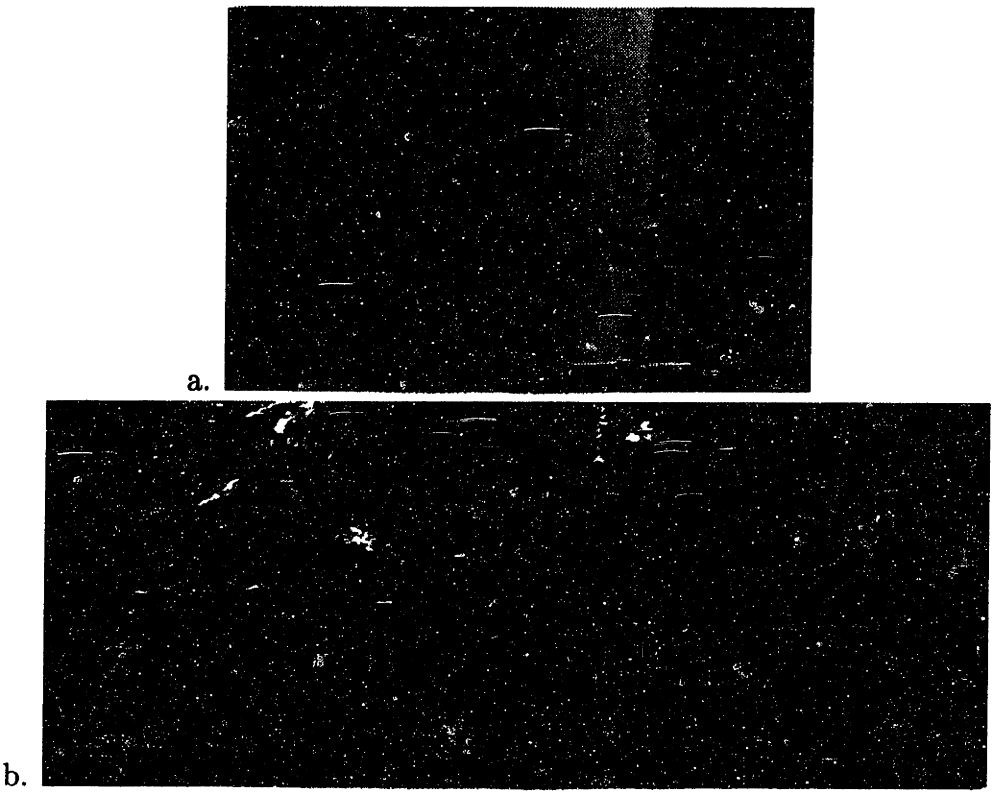

Figure 3-9: End Effects. 40:1 Tapered Oscillating Cylinder without end plate. $R_{\overline{d}} = 1500$, $A/\overline{d} = 0.25$, $S_t = 0.18$.

Chapter 4

Oscillating Tapered Cylinder

4.1 Patterns behind Oscillating Cylinders

The form of the patterns behind a uniform cylinder, forced to oscillate harmonically transversely to an oncoming stream, has been mapped by Williamson & Roshko [55]. The patterns have been found to vary significantly as function of the amplitude and frequency. For a given experiment, the patterns are expected to persist along the entire span when proper care is taken to avoid end effects, for example with the use of sufficiently sized and properly shaped end plates. Inhomogeneities along the span and end effects cause vortex dislocation and oblique shedding phenomena [54].

In contrast to the classic Kármán vortex street behind a non-oscillating cylinder, the patterns in the wake of an oscillating cylinder change depending on the amplitude and frequency of vibration. In studies by Williamson and Roshko, two such patterns seemed to predominate: the '2S' and '2P' patterns. Figure 4-1 maps the occurrence of each pattern within the amplitude-frequency domain.

The '2S' pattern resembles the Kármán vortex street in that one vortex is shed alternately from one side then the other (see figure 4-2a). With the vibrating cylinder each vortex is shed at the maximum amplitude of oscillation such that one vortex is shed per half cycle of oscillation. The vortices have alternate signs maintaining a

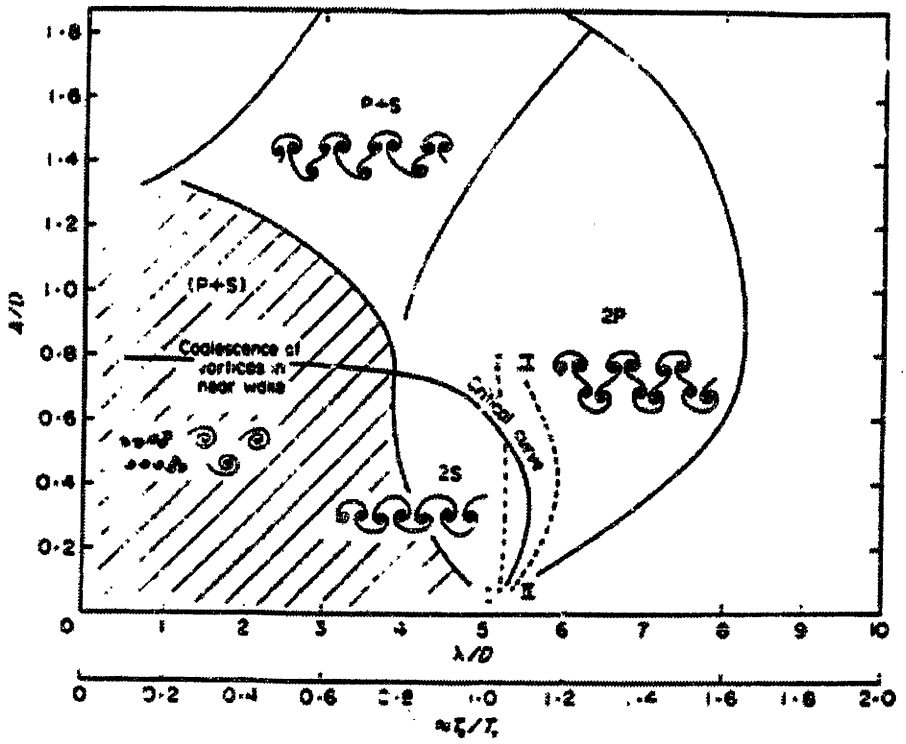

Figure 4-1: Map of vortex synchronization regions in the wavelength-amplitude plane as found by Williamson and Roshko (1988)

stable wake configuration.

The '2P' pattern persists at higher reduced velocity as seen in figure 4-1. Here two vortices of opposite sign are shed per half cycle. Each pair of vortices convect downstream and laterally out from the centerline of oscillation. The '2P' pattern is depicted in sketch (b) of figure 4-2.

The forces on the cylinder change depending upon which pattern prevails. Bishop and Hassan [5] note that along a critical curve in the amplitude wavelength (frequency) domain an abrupt jump in force occurs. This jump in force corresponds with the switch in shedding mode from '2S' to '2P'. While these patterns and force experiments correspond to a uniform cylinder in uniform flow, they can be used to hypothesize what will result for an oscillating tapered cylinder.

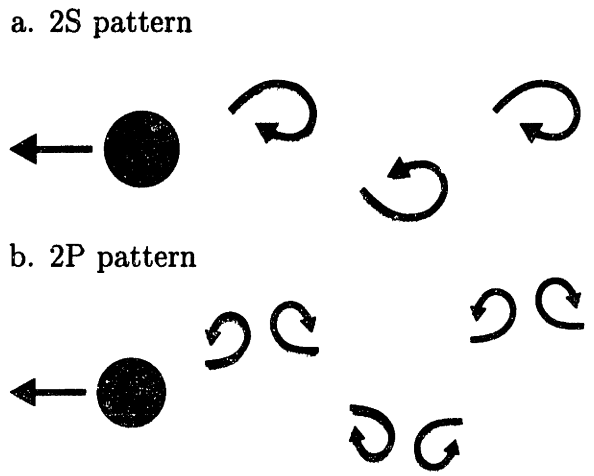

Figure 4-2: Schematic sketch of the three predominate shedding patterns: 2S, 2P. Arrow indicates the direction of rotation for each vortex.

The patterns behind a tapered cylinder can not be expected to compare with those of a uniform cylinder, since its diameter varies along the length; hence, for a given amplitude and oscillation frequency the entire cylinder does not map into one shedding regime in the A/d vs. λ/d plane. This raises the question: what, if any, is the predominant vortical pattern behind an oscillating tapered cylinder, and how does it vary along the span. To address this question, we conducted a systematic set of visualization tests using the tapered cylinder. Above a threshold amplitude and within certain frequency ranges, a single vortical pattern was observed to emerge clearly, and there were no discernible cells of vortex formation; this differs with the results observed behind stationary tapered cylinders [36, 34]. We attribute this difference to the effect of amplitude of vibration, which was also shown by Stansby [42] to alter drastically the length of the forming cells, and to result in the formation of a dominant middle cell.

For certain values of the amplitude of vibration, A/d, and the reduced frequency, fd/U, we observed a *hybrid mode* forming, consisting of, using the nomenclature of Williamson & Roshko [55]: a '2S' mode, i.e. two vortices per cycle, along the part of the cylinder span with the larger diameter; and a '2P' mode, i.e. four vortices per

cycle, for the rest of the span which had smaller diameter. A distinct vortex split separated the two patterns, which had the same frequency and were phase–locked. The hybrid mode was observed throughout the Reynolds number range considered, i.e. between 400 and 1500, based on an average diameter of the cylinder, $\overline{d} = 2.4\ cm$. Lead precipitation and DPIV methods illuminated some interesting features in the wake of the 40:1 tapered cylinder. This phenomenon constitutes a new mechanism peculiar to tapered cylinders in uniform flow, and by extension possibly to uniform cylinders in shear flow.

4.2 Spanwise Visualization

We present results here for cases demonstrating a single dominant pattern along the entire span; as well as cases showing a clear hybrid mode exhibiting pattern transition between '2S' and '2P' mode at a location along the span of the cylinder.

A vertical plane is visualized, which is parallel to the center line of the cylinder (z–axis) and contains the direction of the oncoming flow (x–axis); located at a distance from the average position of the cylinder (along the y–axis) equal to the maximum excursion of the edge of the average section of the cylinder. Results from both the CCD and the VHS camera are shown. Although the lead precipitation images taken using the VHS camera are less clear in detail, they are quite insightful because they show the entire span of the cylinder. Tests shown here are for two different values of the Reynolds number, $R_{\overline{d}} = 400$ and 1,500; three values of amplitude to average diameter ratio, $A/\overline{d} = 0.25$, 0.5, and 1.0; and three values of the reduced frequency, $f^* = 0.162$, 0.18, and 0.198.

In figures 4-3 to 4-7, the tapered cylinder is moving at constant speed from left to right; the images are captured with the CCD camera. The section of cylinder span shown is about five diameters in length, stretching between $z = 9.75\ \overline{d}$ and $z = 14.75\ \overline{d}$.

Figure 4-3 provides two successive snapshots showing the evolution of a '2P' structure. Within the visualized plane of figure (a), two spanwise parallel vortices are observed which have just been formed and can be seen at the center and left of the figure. The parameters for this case are: Reynolds number, $R_{\overline{d}} = 400$, amplitude to diameter ratio, $A/\overline{d} = 1.0$, and reduced frequency $f^* = 0.18$. Several streamwise (or rib) vortices connect in the streamwise direction and wrap around the two main vortices, contorting their shape to appear almost helical. The cylinder has just passed from the position of maximum displacement and is moving towards the center plane. The pair of counter–rotating vortices convects laterally away from the centerline of oscillation, hence figure (b), taken 1.5 s later, shows a different cross–section of the vortices than figure (a). Also, the streamwise vortices have grown stronger in (b), and the spanwise vortices are more contorted.

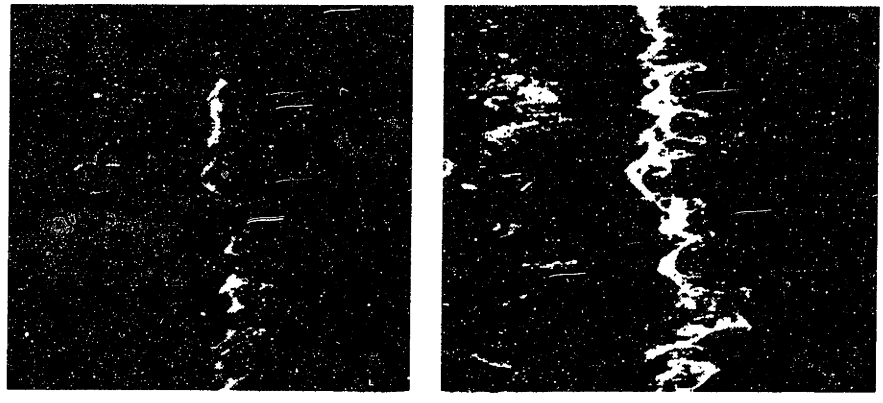

a. b.

Figure 4-3: Evolution of the '2P' shedding pattern for the 40:1 Tapered Oscillating Cylinder. $R_{\overline{d}} = 400$, $A/\overline{d} = 1.0$, $f^* = 0.18$.

Figure 4-4 provides three successive snapshots of the formation of a '2P' structure for higher Reynolds number, $R_{\overline{d}} = 1,500$, amplitude to diameter ratio $A/\overline{d} = 0.25$, and reduced frequency $f^* = 0.162$. The first figure (a) shows the first spanwise vortex being formed as the cylinder has gone through its position of maximum amplitude. Local fluctuations caused by the growth of streamwise structures at the edge of the vortical structure, are apparent. Figure (b), 0.27 seconds (8 frames) later, shows the

same vortex completely formed and located at a new position downstream, while it reveals the emergence of the second spanwise vortical structure, which appears as a thin bright line between the previous vortex and the cylinder. At the next time–step shown in figure (c), 0.5 seconds later, the second vortex has also fully formed, while streamwise structures, about one cylinder diameter apart, take shape connecting and wrapping around the two counter-rotating vortices; these cause the helical contortions in the first vortex to grow.

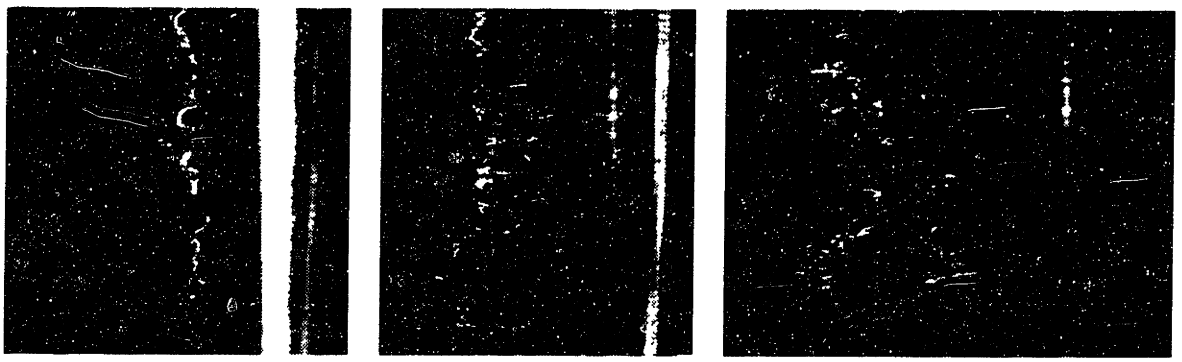

a. b. c.

Figure 4-4: Evolution of the '2P' Shedding Pattern for the 40:1 Tapered Oscillating Cylinder. $R_{\overline{d}} = 1500$, $A/\overline{d} = 0.25$, $f^* = 0.162$.

The influence of the streamwise vortices is also evident in two cases shown in figure 4-5. Shedding is dominated by the '2P' pattern in both cases for $R_{\overline{d}} = 400$. Figure (a) is obtained for $A/\overline{d} = 0.5$ and reduced frequency $f^* = 0.2$; and figure (b) for $A/\overline{d} = 1.0$ and reduced frequency $f^* = 0.162$. In figure (b), adjacent streamwise vortices, which are counter-rotating, provide the appearance of "mushroom" structures superposed on the main vortex line to the right. Also, in figure (b) the first vortex has convected further out of the visualization plane, in the direction away from the average position of the cylinder, and is less clearly visible.

Figure 4-6 depicts three successive snapshots from a case exhibiting hybrid mode formation. The field of view contains the transition between '2S' pattern (upper end, larger diameter) to '2P' pattern (lower end, smaller diameter). Figure (a) shows the

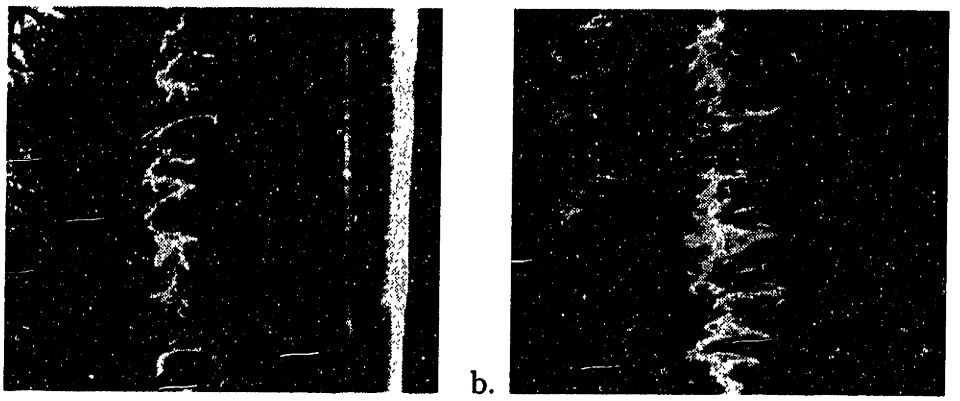

Figure 4-5: 40:1 Tapered Oscillating Cylinder in '2P' mode. (a): $R_{\overline{d}} = 400$, $A/\overline{d} = 0.5$, $f^* = 0.198$; and (b): $R_{\overline{d}} = 400$, $A/\overline{d} = 1.0$, $f^* = 0.162$.

appearance of a first vortex, although there is a marked phase difference in the vortex formation at a point close to the top. The phase difference is caused by the memory effects of previously shed vorticity, which has different structure at the upper and lower cylinder ends. Figure (b) shows that a second vortex has appeared, which, however, extends only to the point where the phase difference was observed in (a). Further up, the second vortex acquires a three–dimensional shape, outside the plane of view and towards the centerline, connecting to a vortex which has the same sign but lies at the opposite lateral edge of the wake. Figure (c) shows the subsequent evolution of the vortical structure, as well as the rib vortices which grow from (a) to (c). The Reynolds number is, $R_{\overline{d}} = 400$, the amplitude to diameter ratio $A/\overline{d} = 0.5$, and the reduced frequency $f^* = 0.198$. A similar vortical structure, formed one period earlier, can be faintly seen at the left edge of figure (c); the process is repeatable from cycle to cycle.

Figure 4-7 depicts the portion of a hybrid mode around the spanwise location of pattern transition, for higher Reynolds number, $R_{\overline{d}} = 1,500$, amplitude to diameter ratio $A/\overline{d} = 0.5$, and reduced frequency, $f^* = 0.18$. The pattern transition is found here at a slightly lower point along the span than in figure 4-6; also, due to the difference in the reduced frequency, the sequence in the formation of the two vortices

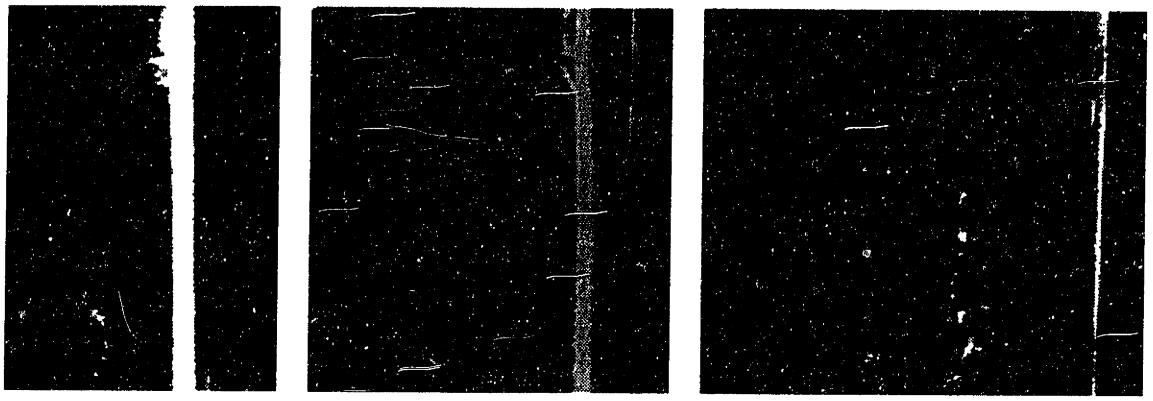

a. b. c.

Figure 4-6: Hybrid mode shown at the spanwise location of pattern transition from '2S' to '2P' pattern. $R_{\overline{d}} = 400$, $A/\overline{d} = 0.5$, $f^* = 0.198$.

is slightly different: in (a) the first vortex is faintly seen, while the second vortex is clearly seen. Images (a) and (b) are 0.12 seconds apart; image (c) is taken during the next oscillatory cycle, 2.2 seconds after (b). Figures (b) and (c) show that the split occurs at roughly the same spanwise location from oscillation to oscillation. These images are very similar in their qualitative features to the previous set of figures, despite the difference in Reynolds number. The appearance of more intense rib vortices is noted.

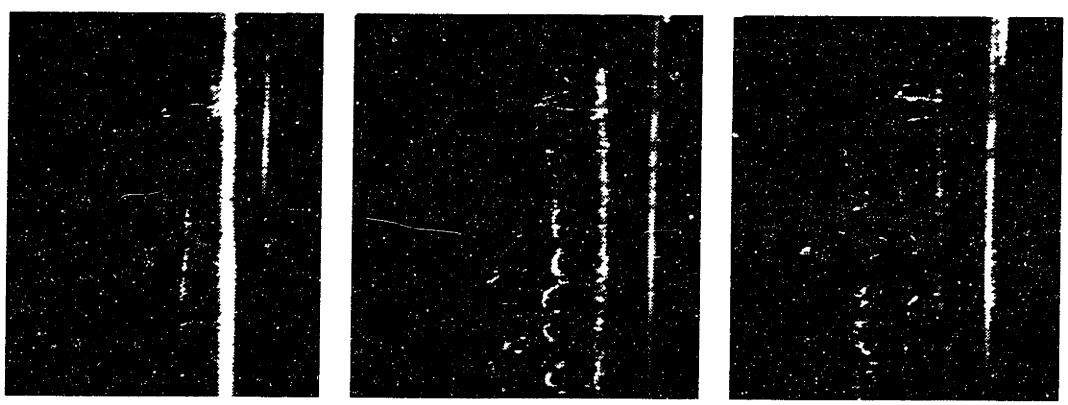

a. b. c.

Figure 4-7: Hybrid mode shown at the spanwise location of pattern transition from '2S' to '2P' pattern. $R_{\overline{d}} = 1500$, $A/\overline{d} = 0.5$, $f^* = 0.18$.

Next, in figures 4-8 through 4-10 we show images captured using the VHS camera. The entire span of the cylinder can be seen in these images.

Figure 4-8 shows lead precipitation images, demonstrating the formation of hybrid modes for: $A/\overline{d} = 0.25$; two Reynolds numbers $R_{\overline{d}}$=400 and 1,500; and three values of the reduced frequency, $f^* = 0.162$, 0.18 and 0.198. Rib vortices provide for a helical contortion of the Karman vortices; otherwise the vortical structure clearly consists of '2S' and '2P' patterns joined through vortex splitting. Previously shed vortices have increasingly more three-dimensional structure and appear less clear; however they retain their original structure. For both values of Reynolds number the location of pattern transition moves towards the lower end as the reduced frequency decreases from a value of 0.162 to a value of 0.198. For Reynolds number 400: for $f^* = 0.162$ the split occurs at $z/\overline{d} = 21.0$, where z is measured from the lower end; for $f^* = 0.18$ at $z/\overline{d} = 20.1$; and for $f^* = 0.198$ at $z/\overline{d} = 17.3$. For Reynolds number 1,500: for $f^* = 0.162$ the split occurs at $z/\overline{d} = 19.8$; for $f^* = 0.18$ at $z/\overline{d} = 16.2$; and for $f^* = 0.198$ at $z/\overline{d} = 15.3$. The heights of the splits were resolved within (plus or minus) one average diameter.

Figure 4-9 shows lead precipitation images, again demonstrating the formation of hybrid modes, for: $A/\overline{d} = 0.5$; two Reynolds numbers $R_{\overline{d}}$=400 and 1,500; and three values of the reduced frequency, $f^* = 0.162$, 0.18 and 0.198. Results are qualitatively similar to the previous cases, shown in figure 4-8, which depicted hybrid modes for a lower amplitude; however, the location of transition shifts to lower spanwise locations, as expected from quasi two–dimensional considerations of the effect of amplitude using the results of Williamson & Roshko [55] for uniform cylinders. Also, the Reynolds number appears to have an effect on the spanwise location of the pattern transition. Again, for both values of Reynolds number the location of pattern transition moves towards the lower end as the reduced frequency decreases from a value of 0.162 to a value of 0.198. For Reynolds number 400: for $f^* = 0.162$ the split occurs at $z/\overline{d} = 23.2$, where z is measured from the lower end; for $f^* = 0.18$ at $z/\overline{d} = 20.7$; and

for $f^* = 0.198$ at $z/\overline{d} = 17.0$. For Reynolds number 1,500: for $f^* = 0.162$ the split occurs at $z/\overline{d} = 21.2$; for $f^* = 0.18$ at $z/\overline{d} = 15.1$; and for $f^* = 0.198$ at $z/\overline{d} = 9.0$.

Figure 4-10 shows lead precipitation images for: $A/\overline{d} = 1.0$; two Reynolds numbers $R_{\overline{d}}$=400 and 1,500; and three values of the reduced frequency, $f^* = 0.162$, 0.18 and 0.198. Streamwise vortices are ubiquitous as before; the vortical structure, however, is definitely of a single mode, '2P', for all parametric values.

In figure 4-11 we present a comparison between the mode transition results of the tapered cylinder, obtained from figures 4-8 through 4-10 herein, and the uniform cylinder results of Williamson & Roshko [55], as function of the amplitude to diameter ratio A/d and reduced velocity V_r. Dashed lines mark the transitions between modes obtained by Williamson & Roshko. We provide the combinations of A/d and $V_r = U/(fd)$ corresponding to the ends of the tested cylinders for each experiment, where the actual diameter d is used, and we mark the type of vortex pattern observed: The smaller diameter end is marked by the 'o' symbol, and the larger diameter end by the '*' symbol. For the cases where a hybrid mode is observed we mark the corresponding location of the vortex split, based on the local diameter. Because the split can be identified within one diameter (plus or minus) and there is Reynolds number dependence, we provide a shaded patch rather than a discrete line. As seen, there is reasonable agreement between the data obtained for the linearly tapered cylinders herein, and the uniform cylinder data of Williamson & Roshko.

4.3 Visualization at Planes Perpendicular to the Cylinder Axis

Visualization across planes perpendicular to the cylinder axis, i.e. $x - y$ planes, are recorded to compare with the patterns observed behind uniform cylinders. The lead precipitation method and DPIV were employed for this purpose. In the cases using lead precipitation, the tank was also seeded with fluorescent particles used in

DPIV, which enhanced the visualization process and allowed several of the cases to be processed using the DPIV algorithm. Using the vertical images ($x - z$ plane) as a reference, perpendicular ($x - y$ plane) slices were taken above and below the transition in shedding mode. Both Reynolds numbers 400 and 1500 showed distinct '2S' and '2P' patterns, above and below the transition, respectively. An additional set of experiments, at the intermediate Reynolds number 800 was also investigated for comparison.

At the two lower Reynolds numbers, 400 and 800, the formation and evolution of the two patterns was clear. For $R_{\overline{d}} = 1500$ the presence of Bloor vortices was noted, making visualization less clear; yet the two different patterns can still be established unambiguously.

Figure 4-12 provides two snapshots of the formation of a '2P' mode for $R_{\overline{d}} = 1,500$, $A/d = 0.5$, $f^* = 0.18$ showing Bloor vortices forming on the layers emanating from the cylinder. In image (a) the slice is at $z/\overline{d} = 6.5$, well below the pattern transition region. The image is taken when the cylinder has fully traversed through its maximum oscillation and shed a pair of counter–rotating vortices. Image (b) is at $z/\overline{d} = 10.4$, still below the pattern transition, and taken when the cylinder has passed through the minimum oscillation and shed a pair of counter rotating vortices at the opposite wake side than shown in image (a).

Figure 4-13 shows the formation of '2P' mode at $R_{\overline{d}}$=400, $A/d = 0.5$, and $f^* = 0.18$. Figure (a) shows the beginning of shedding a pair of primary vortices at the upper edge of the wake: The first vortex is rotating counter–clockwise and the second vortex, closest to the cylinder, is rotating clockwise. The cylinder has just passed through its maximum oscillation. Image (b) shows a later time step for the same parametric values, as a pair of vortices is almost completely shed at the lower edge of the wake. The cylinder is traveling from the point of minimum excursion towards the centerline of oscillation. Here, coincidentally, a streamwise vortex has been captured as a bright line connecting two clockwise rotating vortices (the second and third

vortices, counting as one moves downstream from the cylinder). The streamwise vortex is clearly visible when the video recording is played back; in still photographs it makes the depiction of the primary vortical patterns less clear (for example, the third vortex is almost indistinguishable).

Next we provide DPIV images obtained at planes transverse to the cylinder axis. They depict modes dominated by a single pattern as well as hybrid modes.

Figure 4-14 shows (a) the velocity and (b) the vorticity fields, obtained through DPIV and corresponding to $R_{\overline{d}} = 1,500$, $A/\overline{d} = 0.5$, and $f^* = 0.18$. A '2P' pattern is clearly seen in the vorticity map (b). The red color represents positive vorticity, counter-clockwise rotation of the fluid; and the blue spots show negative vorticity, clockwise rotation of the flow. The laser sheet was placed below the pattern transition region at a height: $z/\overline{d} = 6.7$. Here the cylinder has passed through its minimum oscillation and is moving up towards the centerline.

Figure 4-15 also shows velocity and vorticity plots corresponding to a '2P' pattern, obtained for $R_{\overline{d}} = 400$, $A/\overline{d} = 0.5$, and $f^* = 0.18$. This plane, at $z/\overline{d} = 4.2$, captured the presence of a streamwise structure connecting the clockwise rotating vortices of each pair. While the video obtained shows this feature quite clearly, the instantaneous snapshot does not suggest a true '2P' pattern.

Figure 4-16 shows plane cuts of the velocity and vorticity fields for slices depicting a hybrid mode. Two horizontal slices have been processed, one obtained at $z/\overline{d} = 22.9$ (figures a and b), and the other at $z/\overline{d} = 7.9$ (figures c,d). The parameters are: Reynolds number 1,500, $A/\overline{d} = 0.5$, and $f^* = 0.198$. The vorticity field shown in figure (b) shows that the upper portion of the cylinder in this case is shedding a '2S' pattern, whereas the lower slice (figure d) shows a '2P' pattern; both figures are in complete agreement with the lead precipitation results.

Figure 4-17 shows velocity and vorticity plots depicting a hybrid mode for different conditions than shown in figure 4-16: $R_{\overline{d}} = 1500$, $A/\overline{d} = 0.5$, and $f^* = 0.18$. The two slices are located at different heights: $z/\overline{d} = 18.7$ (figures a and b) and $z/\overline{d} = 6.7$

(figures c and d). Again, as in the previous set of figures, the upper slice depicts a '2S' pattern and the lower slice shows a '2P' pattern of shedding.

We used the velocity and vorticity plots to obtain estimates of the circulation of the vortices. This is done by integrating the vorticity inside a circular area whose center is chosen to be within the core of the vortex, while its radius is incrementally increased until the circulation value levels off within a pre–set tolerance. Circulation in the '2S' mode (figure b) for the clockwise vortex with its core located at $x/d = 2.8$ is $\Gamma_s = -22.13\ cm^2/s$. For the '2P' mode (figure d), for the clockwise vortex with its core at $x/d = 2$ we find $\Gamma_{p1} = -6.3\ cm^2/s$, and for the clockwise vortex with its core at $x/d = 4$ we find $\Gamma_{p2} = -18.56\ cm^2/s$; hence the sum circulation for the two clockwise vortices in the '2P' pattern is $\Gamma_p = -25.89\ cm^2/s$. In accordance with the lead precipitation results, the two clockwise vortices from the '2P' mode considered above, connect to the single clockwise vortex from the '2S' vortex at the location of the vortex split. Given the distance between the two slices and the uncertainty in evaluating the circulation, the calculation supports the suggested topology of the vortical structure.

4.4 Vortex Dislocation and Reconnection

Vortex dislocations, (also called vortex splitting), i.e. the strong localized distortions of a spanwise vortex and its connection with two or more vortices, have been studied by Gerrard [15], Eisenlohr & Eckelmann [11], Williamson [52] and Zhang & al. [59]. Williamson [52] has shown that vortex dislocations account for intermittent low–frequency oscillations in the wake. Such vortex dislocations are generated between adjacent spanwise cells of different frequency and cause momentary difference in shedding phase of the primary vortices between cells. Cells are caused, for example, by cylinder inhomogeneities and by end conditions.

Figure 4-18 provides a sketch of the topology of primary vortex reconnection as

it emerges from the lead precipitation results. The figure shows a snapshot in the hybrid mode formation; the details of the individual '2S' and '2P' pattern formation and evolution, at sections lying at least two diameters away from the vortex split location, resemble closely the corresponding patterns shown by Williamson & Roshko for uniform cylinders.

4.5 Summary

Flow visualization behind a linearly–tapered, oscillating cylinder, with average diameter $\overline{d}$ and taper ratio 40:1, was conducted at Reynolds numbers in the range 400 through 1,500. The results reveal that within a certain parametric range a *hybrid mode* forms, consisting of the simultaneous formation of two different primary vortical patterns along the span of the cylinder: (a) two vortices per cycle ('2S' pattern) along the part with the larger diameter; and (b) four vortices per cycle ('2P' pattern) along the part with the smaller diameter. The transition between the two patterns occurs at a specific spanwise location, whose position depends on the amplitude to diameter ratio $A/\overline{d}$, the reduced frequency $f^* = f\overline{d}/U$, and the Reynolds number $Re_d = U\overline{d}/\nu$. The two patterns of the mode are phase locked, and the mode is periodic and persistent, hence there is no low-frequency forcing; in this sense it is different than the vortex dislocation observed behind non–uniform cylinders, such as reviewed in Williamson [54]. A vortex connection mode is suggested on the basis of lead precipitation and DPIV data.

Outside the range of hybrid mode formation clean '2S' or '2P' modes are observed. Rib vortices are ubiquitous for all Reynolds numbers considered, irrespective of amplitude and frequency of oscillation, or the specific mode of vortex shedding.

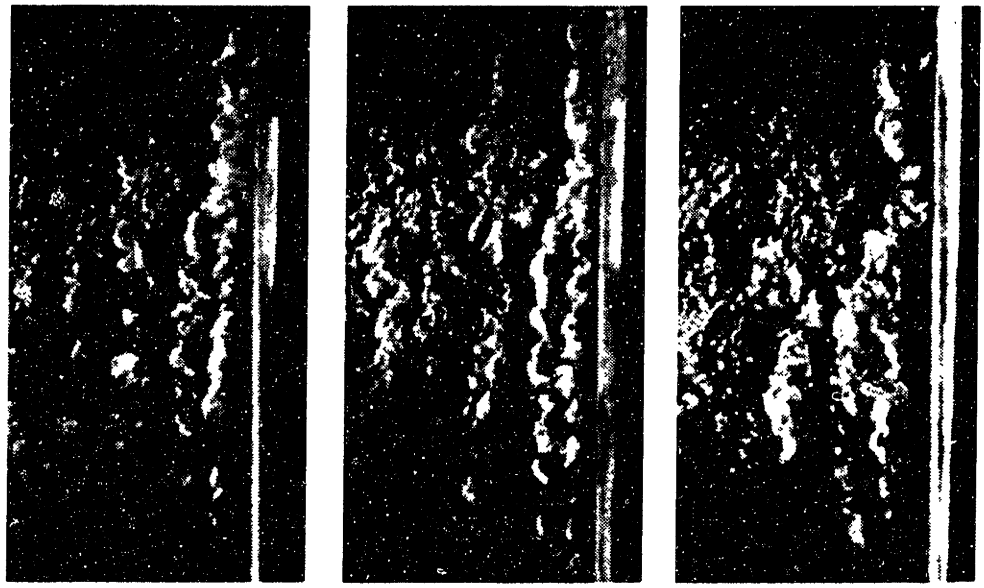

a. $R_{\overline{d}}$=400, f^*=0.162 b. $R_{\overline{d}}$=400, f^*=0.18 c. $R_{\overline{d}}$=400, f^*=0.198

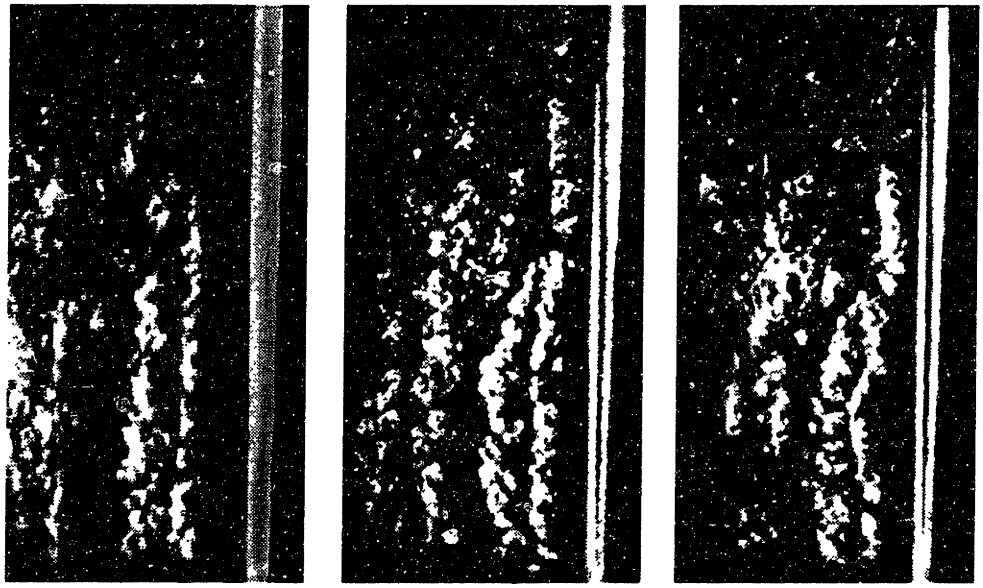

d. $R_{\overline{d}}$=1500, f^*=0.162 e. $R_{\overline{d}}$=1500, f^*=0.18 f. $R_{\overline{d}}$=1500, f^*=0.198

Figure 4-8: Lead Precipitation visualization showing the entire cylinder span for $A/\overline{d} = 0.25$.

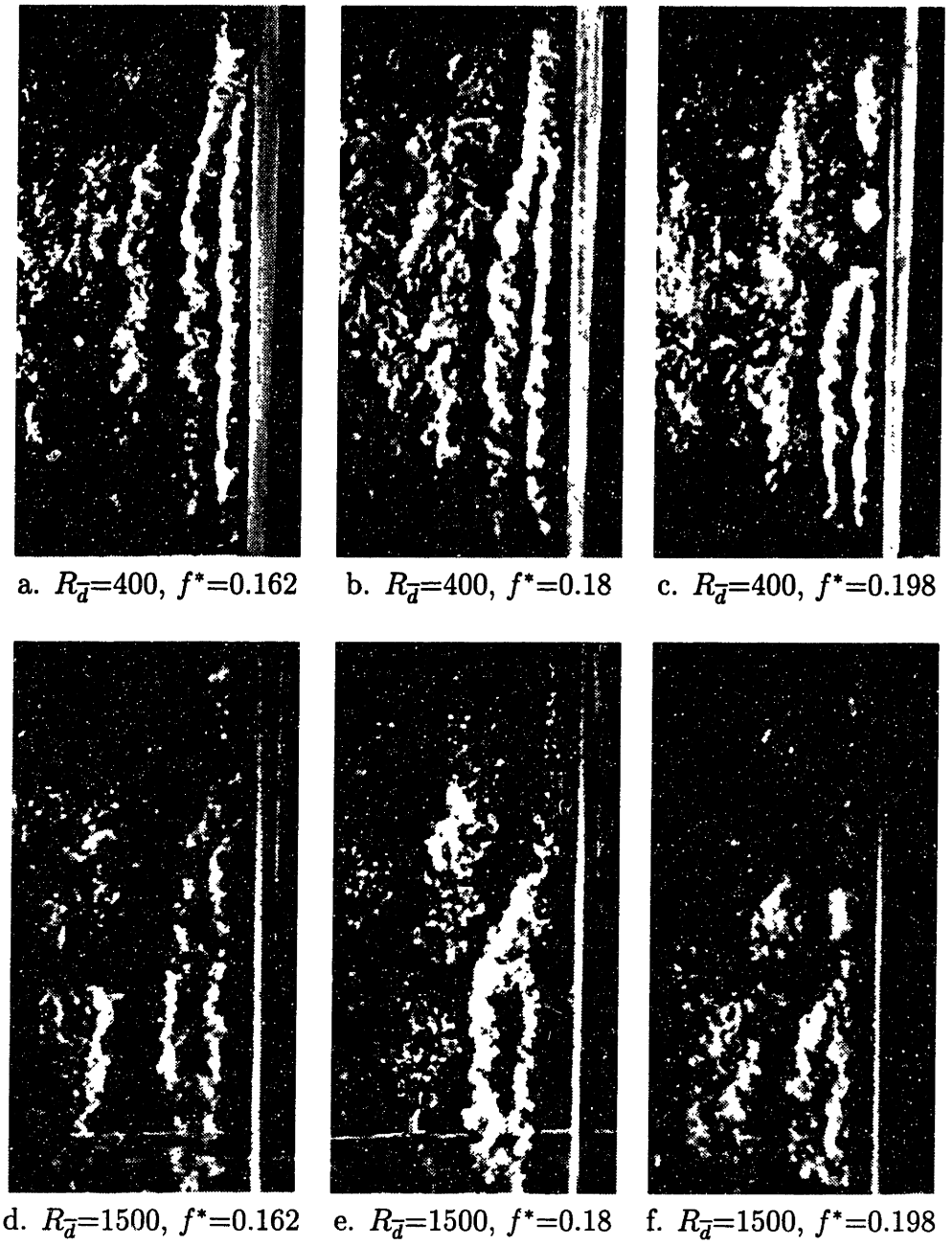

a. $R_{\overline{d}}$=400, f^*=0.162 b. $R_{\overline{d}}$=400, f^*=0.18 c. $R_{\overline{d}}$=400, f^*=0.198

d. $R_{\overline{d}}$=1500, f^*=0.162 e. $R_{\overline{d}}$=1500, f^*=0.18 f. $R_{\overline{d}}$=1500, f^*=0.198

Figure 4-9: Lead Precipitation visualization showing the entire cylinder span for $A/\overline{d}$ = 0.5.

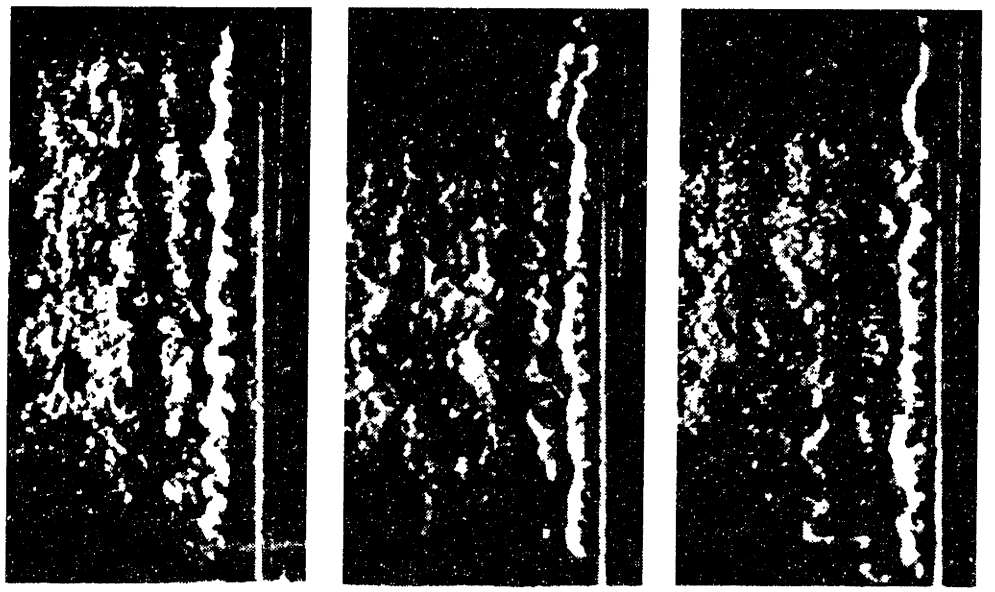

a. $R_{\overline{d}}$=400, f^*=0.162 b. $R_{\overline{d}}$=400, f^*=0.18 c. $R_{\overline{d}}$=400, f^*=0.198

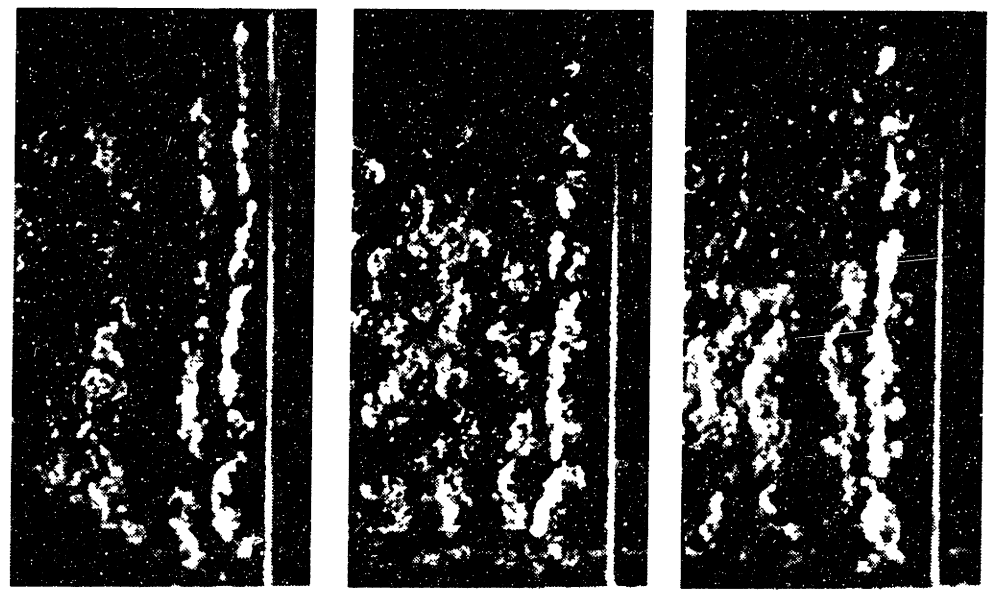

d. $R_{\overline{d}}$=1500, f^*=0.162 e. $R_{\overline{d}}$=1500, f^*=0.18 f. $R_{\overline{d}}$=1500, f^*=0.198

Figure 4-10: Lead Precipitation visualization showing the entire cylinder span for $A/\overline{d} = 1.0$.

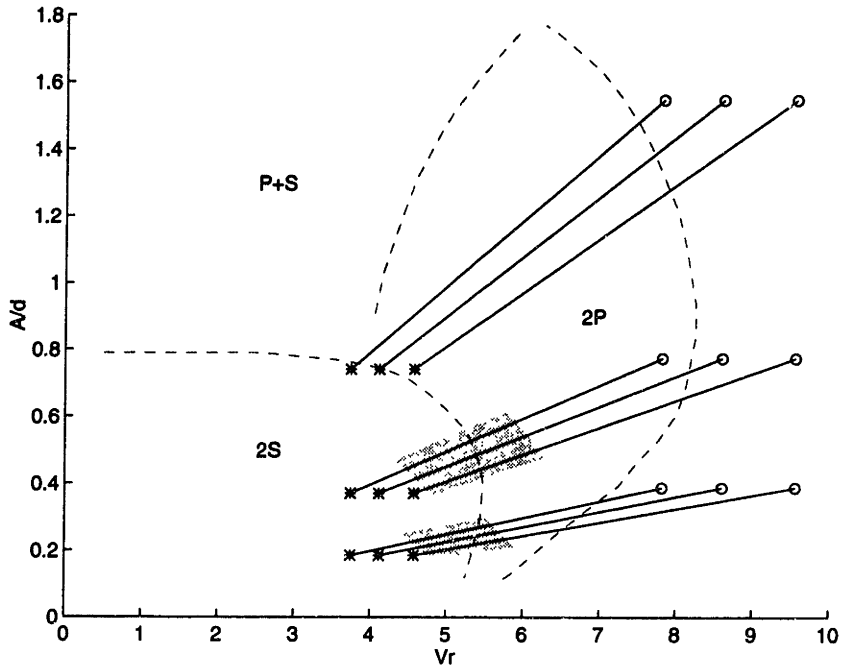

Figure 4-11: Range of reduced velocity versus amplitude to diameter ratio for the 40:1 Tapered cylinder experiments. (*) indicates the larger end of the cylinder and (o) the smaller end. The shaded region represents the area of the switch in shedding mode for both Reynolds number cases: 400 and 1500.

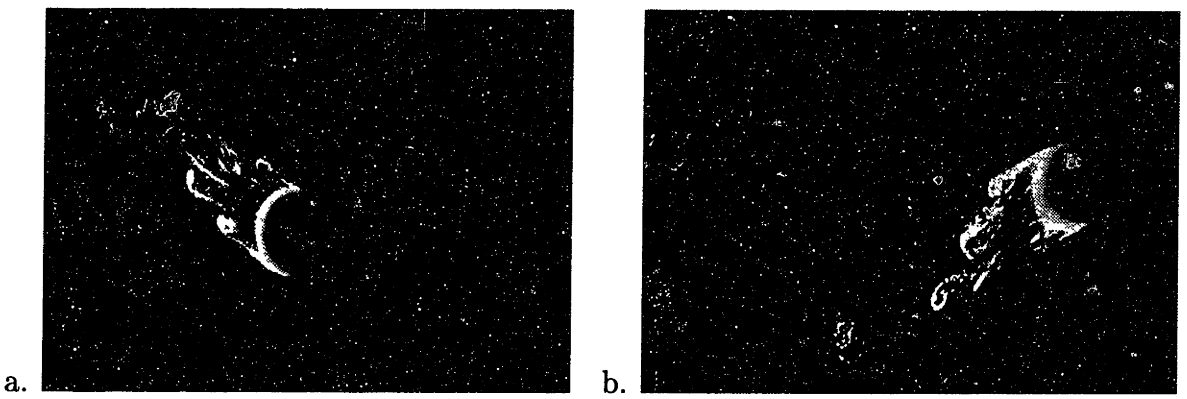

Figure 4-12: Bloor Vortices forming at $R_{\overline{d}} = 1500$, associated with a '2P' pattern.

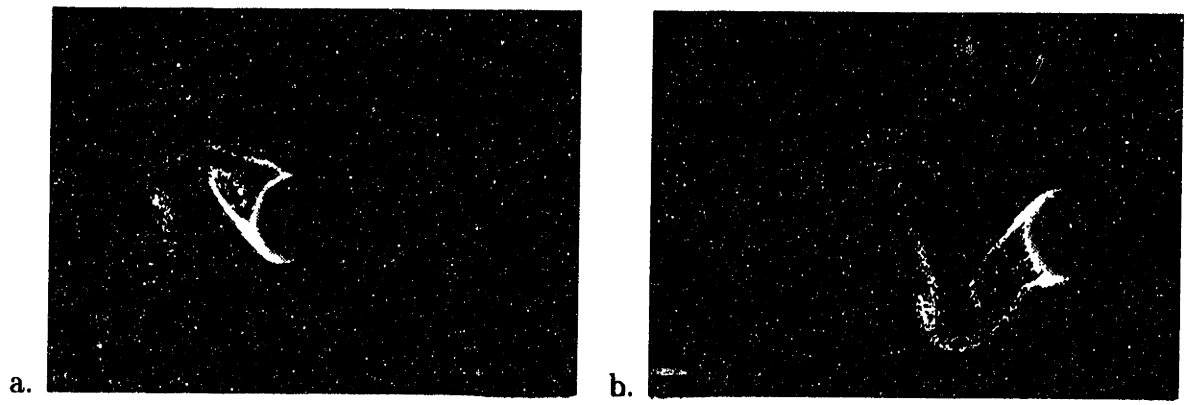

Figure 4-13: '2P' shedding mode at $R_{\overline{d}} = 400$. Image (a) shows the formation of a vortex pair in a '2P' pattern. Image (b) is taken at a later time, showing a braid vortex in the field of view, which connects two clockwise rotating vortices.

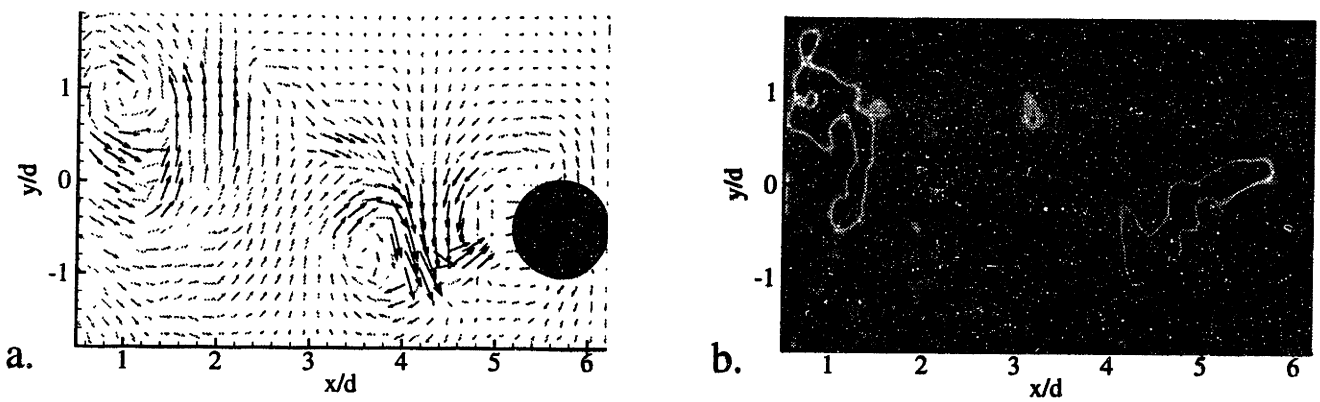

Figure 4-14: Velocity (a) and vorticity (b) plots showing a '2P' pattern for $R_{\overline{d}} = 1500$, $A/\overline{d} = 0.5$, and $f^* = 0.18$. The horizontal slice is imaged at $z/\overline{d} = 6.7$.

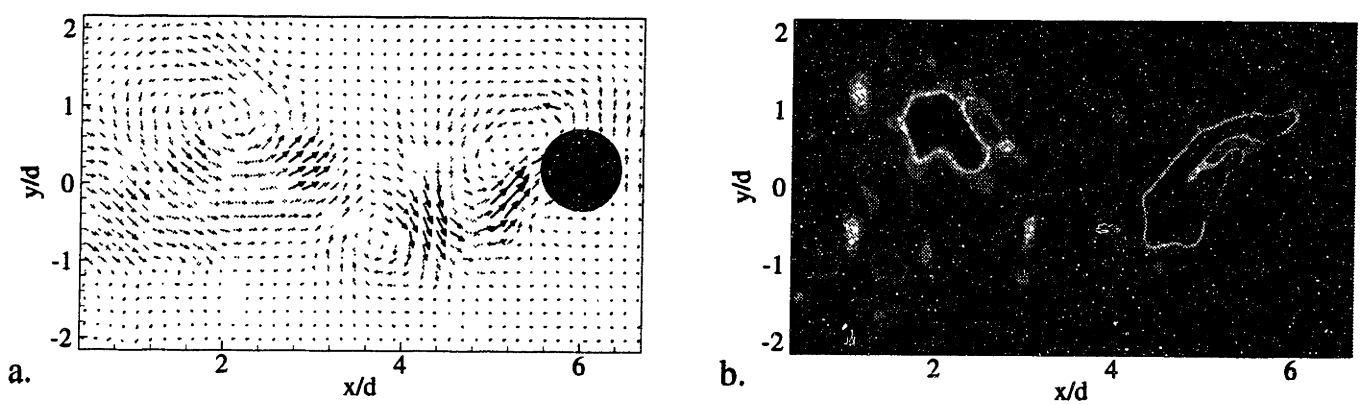

Figure 4-15: Velocity (a) and vorticity (b) plots showing a '2P' pattern for $R_{\overline{d}} = 400$, $A/\overline{d} = 0.5$, and $f^* = 0.18$. The horizontal slice is imaged at $z/\overline{d} = 4.2$.

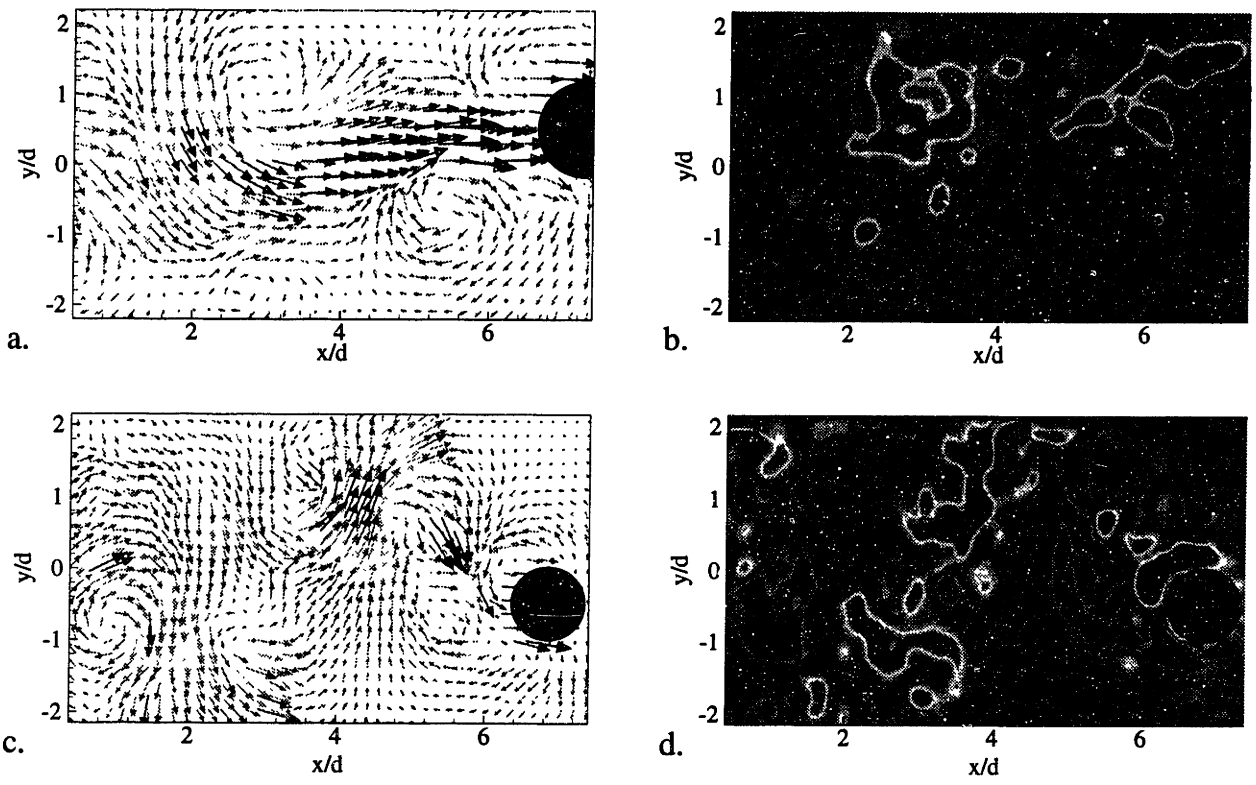

Figure 4-16: Velocity and vorticity plots: at $z/\overline{d} = 22.9$ (a and b); and at $z/\overline{d} = 7.9$ (c and d); for $R_{\overline{d}} = 1500$, $A/\overline{d} = 0.5$, and $f^* = 0.198$.

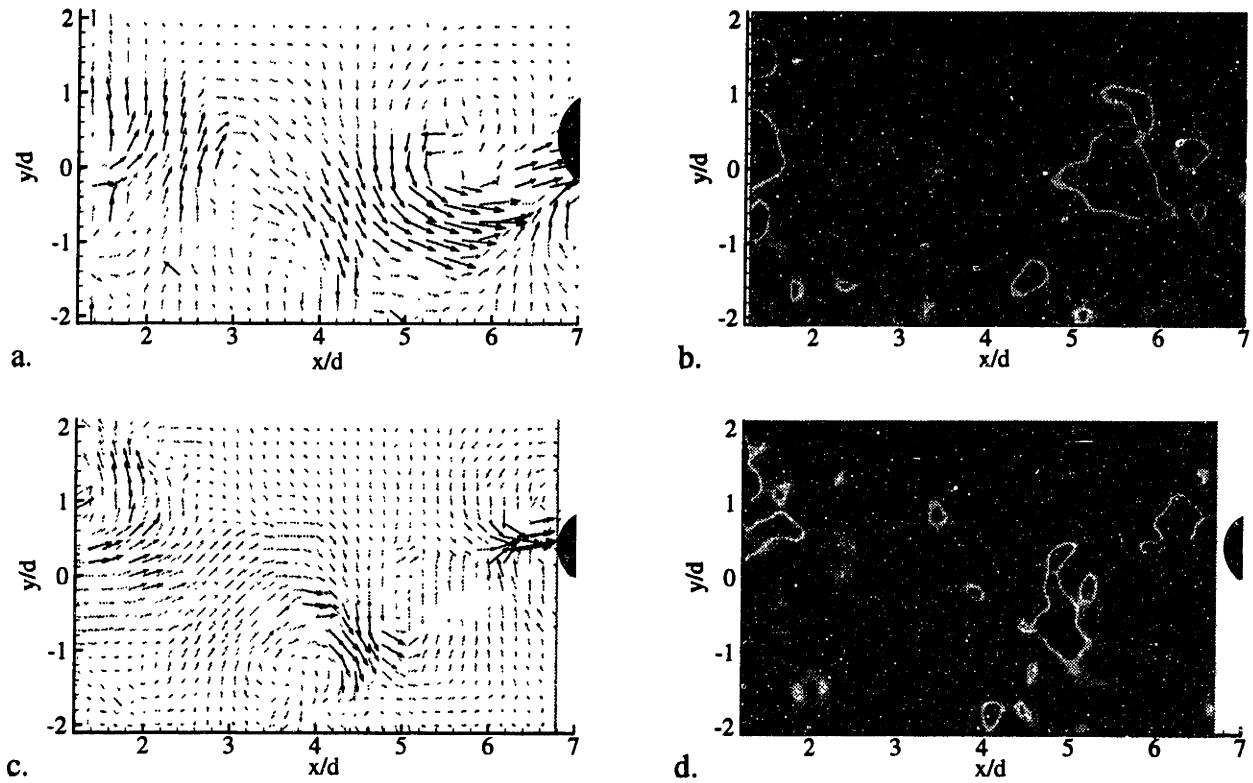

Figure 4-17: Velocity and vorticity plots: at $z/\overline{d} = 18.7$ (a and b); and at $z/\overline{d} = 6.7$ (c and d); for $R_{\overline{d}} = 1500$, $A/\overline{d} = 0.5$, and $f^* = 0.18$.

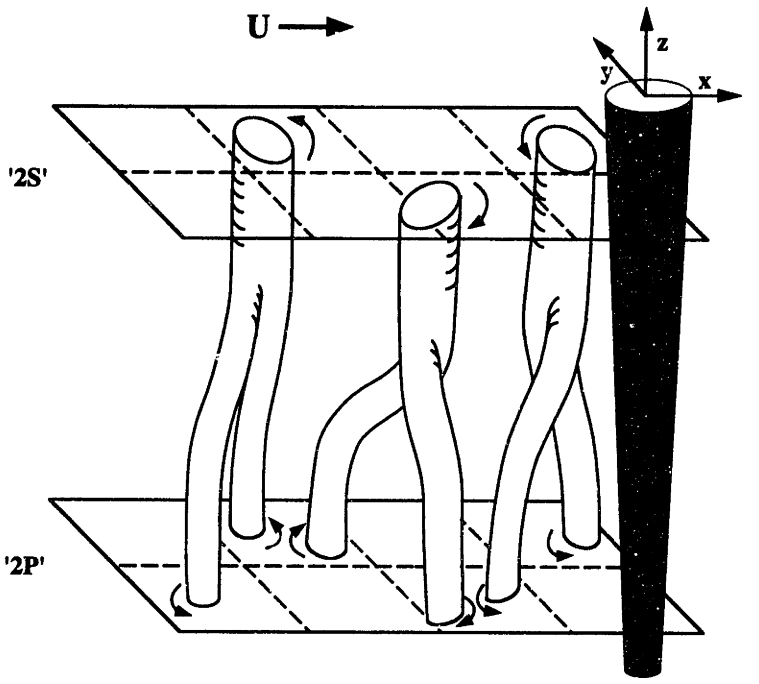

Figure 4-18: Suggested topology of the vortex reconnection between the '2S' and '2P' modes.

Chapter 5

Force Measurements

Force measurements were conducted to compliment visualization results and to help us to assess the impact of the observed fluid phenomenon on the vortex induced forcing mechanisms.

The need to generate a complete experimental force data base for predicting vortex induced vibrations of slender structures has led to testing of cylinders undergoing forced oscillations. Several investigators, including Bishop & Hassan [5], Sarpkaya [39], Staubli [43], Gopalkrishnan [16] and Gopalkrishnan et al. [17] have measured the forces on finite–span oscillating cylinders forced in harmonic, as well as multi–frequency motion. In harmonic tests the transverse (lift) force is decomposed into two components: one in phase with velocity and the other in phase with acceleration. The former is important in determining the range where self–excited oscillations occur; the second is used to derive a value for the added mass coefficient.

Predictions using forced-vibration data with a structural model have been compared against free vibration tests (Staubli [43], Parkinson [35], Sarpkaya [40]): There are parametric regions where such comparison is successful, and other regions where discrepancies are observed. The question of whether forced cylinder experiments can be used to predict free vibrations of cylinders is still open. For example, Griffin [19] compared the wakes of two identical cylinders, one self–excited and the other forced

to oscillate. He did not find essential differences in the global parameters of the wake, although he noted differences in the velocity signal of the free–oscillation wake, which contained more random oscillations. Newman & Karniadakis [33] find through numerical simulation essential differences in the wake structure of a cable forced to oscillate, versus the wake of a self–excited cable. The explanation may be based on the dynamics of the wake; for example, it is known from the study by Nakano & Rockwell [31] that amplitude modulation is capable of altering the wake form. A freely vibrating cylinder can have a different wake structure (and force signal) since it can deviate from a purely harmonic motion.

Data presented in this thesis are in agreement with those of Feng [12], Brika & Laneville [8], and Khalak & Williamson [27]. In addition, we use the two simultaneously recorded end forces directly, to assess spanwise correlation of the fluid structure for the four cases of: *a*) a uniform cylinder in free-vibration, *b*) a uniform cylinder in forced vibration, *c*) a 40:1 tapered cylinder in free-vibration, and *d*) a 40:1 tapered cylinder in forced vibration. Through the force feedback mechanism, we are able to compare force responses in forced sinusoidal motions and free vibrations with the same apparatus and under identical flow conditions. Measurements from the uniform cylinder are detailed in Hover, et al. [24], whereas the results from the tapered cylinder are discussed in the next sections.

5.1 Experimental Considerations

Forces are measured at both ends of rigid cylinders with span 60 *cm*, performing transverse oscillations within an oncoming stream of water, at Reynolds number $Re \approx 3,800$. Forced harmonic motions and free vibrations of uniform and tapered cylinders are studied. To study free motions, a novel force-feedback control system has been developed, consisting of: *(a)* a force transducer, which measures forces on a section of a cylinder moving forward at constant speed; *(b)* a dedicated computer using

the measured force signal real–time to drive a numerical simulation of an equivalent mass–dashpot–spring system; *(c)* a servomotor and linear table which impose, also in real–time, the numerically calculated motion to the cylinder section. The apparatus allows very low equivalent system damping and strict control of the parametric values and structure of the equivalent system.

The cross-correlation of the end forces is formulated as:

$$F_c = \frac{< F_1(t), F_2(t) >}{\sqrt{< F_1(t), F_1(t) >< F_2(t), F_2(t) >}}. \tag{5.1}$$

Calculation of the cross-correlation coefficient between the forces at the two ends of the uniform cylinder reveals five distinct regimes as function of the reduced velocity V_r: Two regimes, for low and high values of V_r, respectively, and far away from the value of $V_r = V_{rS}$ corresponding to the Strouhal frequency, show small correlation; two regimes immediately adjacent to, but excluding V_{rS}, show strong correlation, close to 1; surprisingly, there is a regime containing the Strouhal frequency, within which correlation is low [24]. Free vibrations with a 40:1 tapered cylinder show qualitatively similar results, but the regime containing the Strouhal frequency stretches to higher reduced velocities, while lock-in starts at lower reduced velocities.

When comparing the amplitude and phase of the lift coefficient measured for free and then for forced vibrations, we obtain close agreement for both the tapered and uniform cylinders. When comparing the cross-correlation coefficient, however, we find that it is much higher in the forced oscillations, especially for the uniform cylinder. Hence, although the force magnitude and phase may be replicated well in forced vibrations, the correlation data suggests that differences exist between free and forced vibration cases.

5.2 Forced Vibrations of the Tapered Cylinder

We performed a reduced set of forced vibrations with the 40:1 tapered cylinder to explore the mapping of forces between free and forced vibrations. Figure 5-1 shows a summary view of forces on the cylinder, for A/d values of 0.6 and 1.1, and a range of V_r. At each amplitude, both lift coefficients are strongly negative at low V_r, but increase to near zero above $V_r = 7.0$. In contrast with the uniform cylinder results, there were no tests yielding positive lift coefficients. More noteworthy, however, is that the force correlations in the tapered cylinder in forced-oscillations match the free-vibration results somewhat better than the uniform cylinder [24], especially at $A/d = 0.6$: A comparison of Figure 5-1 with Figure 5-3 shows the similarity of these points. Transitions occur at the same reduced velocity ($\simeq 5.75$), and the primary difference is the minimum value F_c achieves, 0.28 for the free vibration, and 0.58 for the forced vibration.

As in the case of the uniform cylinder forced-oscillation tests discussed in Hover et. al [24], larger amplitudes tend to correlate the forces.

5.3 Free Vibrations of a 40:1 Tapered Cylinder

We conducted tests for similar parametric values with a 40:1 tapered cylinder, with mass ratio 4.0. The ratio $\tau = 40 : 1$ represents the ratio of the cylinder length l to the difference in diameters between the two ends, d_{max}, d_{min}, as was defined in equation 2.1.

Figure 5-2 illustrates that a broad variation from the uniform cylinder results exists. In general, an averaging with respect to reduced velocity seems to occur [25]. The hysteretic jump near $V_r = 6.0$ has apparently vanished and the force correlation varies more gradually, and through only several regimes (figure 5-3). Uniform cylinder force correlations, by comparison, appear to be alternately well-correlated or poorly-correlated, with discontinuous transitions [24].

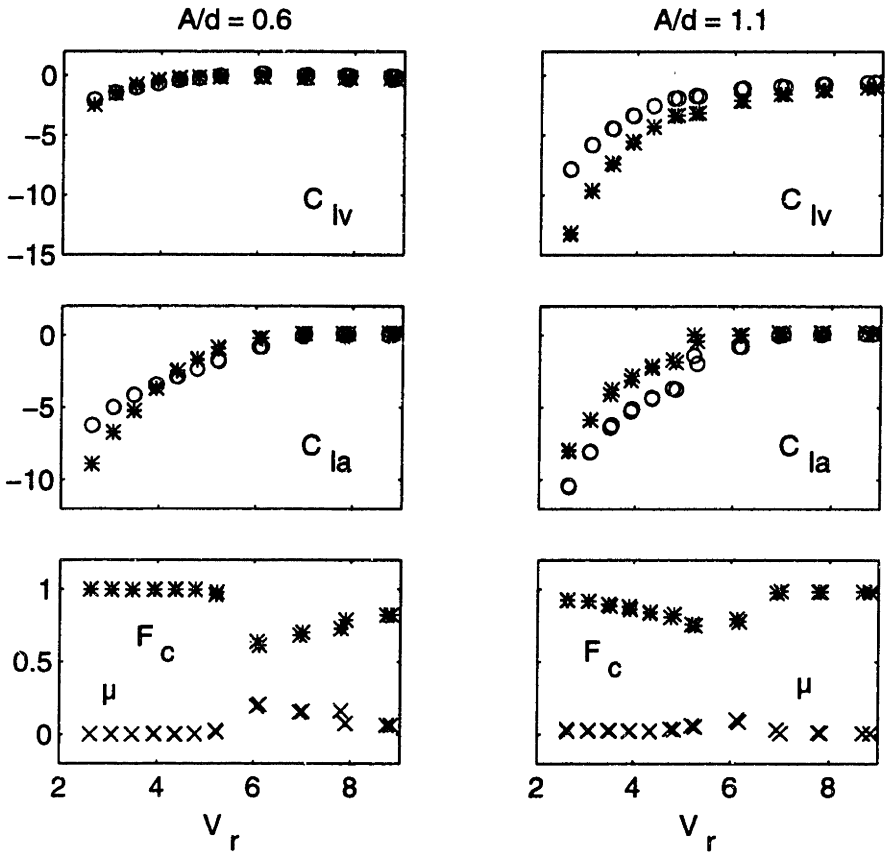

Figure 5-1: Forced-oscillation tests with a 40:1 tapered cylinder. In C_{lv} and C_{la}, '*' denotes the small end of the cylinder, 'o' denotes the larger end.

In the plots, force normalizations are with respect to the two end diameters of the section, so that zero power flow again holds, when each coefficient is multiplied by its appropriate diameter. The lift coefficients show clear separation between forces acting at the smaller end and the larger end of the test section. Lift in phase with acceleration at the smaller end follows a path similar to the uniform case, with the exception that the minimum value is only -1.3 (compare with 3.0). At the larger end, a minimum value of -1.9 is observed at $V_{rn} = 4.5$. At $V_{rn} = 3.5$, a discontinuity in C_{la} is evident, although some scatter in the data exists below $V_{rn} = 4.0$.

The tapered cylinder does not follow the synchronization curve of the uniform cylinder. Below $V_{rn} = 3.0$, an extremely high sensitivity to structural mode exists; it is at this same point that lock-in first begins, but only to about ninety percent of the structural frequency. As V_{rn} increases, the observed frequency moves gradually up to about 1.2, the final value observed in the plots for the uniform cylinder shown in [24].

In a second set of free vibration tests with the 40:1 tapered cylinder, results were similar to those found above. In these tests two different mass ratios, $m^* = 5$ and 10, were investigated for damping parameters between 0.0 and 0.1 ($\zeta = 0.00$, 0.01, 0.02, 0.05, 0.10). Figure 5-4 shows the heave amplitude achieved for these mass ratio and damping parameters resembled that for $m^* = 4$. The maximum A/d achieved was around 0.9 for a reduced velocity of 6.5-7.0. As expected the amplitude decreased with increased damping. Through the range of reduced velocities investigated, the response varied gradually and did not reveal the hysteretic jump as is seen in the case of the uniform cylinder.

The force correlation data, in figure 5-5, shows well correlated end forces between $V_{rn} = 3.0$ and 6.0 ($F_c = .09$). A minimum correlation is seen around $V_{rn} = 7.0$. For the case of mass ratio 5 and damping parameter 0.05, the end forces remain uncorrelated ($F_c = 0.0$ to -0.05) through a range of reduced velocities: 6.0–9.0, and jump back up to $F_c = 0.4$ at $V_{rn} = 9.5$. For $m^* = 5$ and $\zeta = 0.1$, F_c quickly falls off after $V_{rn} = 4.0$ and eventually levels out around $V_{rn} = 7.0$ at a correlation value of 0.2. This is lower than the rest of the cases which seem to level out to a higher correlation value of 0.4. To further understand this feature more tests need to be done in conjunction with flow visualization.

The lift coefficient in phase with acceleration shows similar trends for $m^* = 4$, 5, and 10 (see figure 5-6). The minimum C_{la} is achieved at a higher V_{rn} for $m^* =$ 5, and 10 ($V_{rn} = 4.5$ and 5.0 respectively) compared to $V_{rn} = 4.0$ for $m^* = 4$. The minimum lift coefficient corresponds to higher correlation in end forces. For $m^* = 5$,

the minimum lift coefficient at the large and small ends is -0.9 and -1.3 respectively; and for $m^* = 10$ the minimum $C_{la} = -0.9$ for the large end and -1.5 for the small end. The lift coefficient in phase with velocity is shown in figure 5-7, and the phase change between the forces and the cylinder position in figure 5-8 for reference.

Figure 5-9 shows displacement and force spectra for reduced velocities one through ten, which also covers the uniform cylinder cases. Starting at the lower end, the force signals occupy two distinct and broad ranges, consistent with two different fixed-cylinder shedding rates resulting from two diameters. The wake forces in this region are reasonably well-correlated. Some signature of the second harmonic, again broadband, emerges at $V_r = 2.0$, while the displacement is largely unchanged. The spectral content of the displacement sharpens and aligns closely with that of the forces, at $V_r = 3.0$. At this point also, the correlation between forces is solidifying. Both the displacement and force spectra remain remarkably narrow-band for all reduced velocities between 4.0 and 7.0. Beyond this range, a broadening of the force spectra occurs; the uniform cylinder recovers the fixed-cylinder shedding rate in this higher range.

5.4 Discussion

The use of a force-feedback system solves several of the major problems associated with free-vibration tests. First, the apparatus allows for low-mass tests; the only real limit is the mass of the test cylinder, which dictates the magnitude of the inertial correction. This inertial correction is inherently destabilizing, so the critical constraint is that $m - m_{cylinder} > 0$. Secondly, force and displacement measurements invoke various fittings and wiring. By using a servo-controlled approach, the effects of these connections on the dynamic response of the system can be eliminated. Third, this apparatus allows for both forced and free vibration testing under identical conditions, since only a software change is required. The nature of the feedback system, as noted

previously, also can provide multi-mode and nonlinear structural models: preliminary work with multi-mode models has been reported by Hover *et al* [23]. One critique of the system might be the small phase loss incurred by filtering the force signals. However, the data, which match previously-reported results closely, suggest that this is a minor deficiency.

Recording integrated end forces separately brings about a new element in studying the flow. For the uniform cylinder, the loss of force correlation between Regions *II* and *IV*, which are often associated with '2S' and '2P' flow structure, is indicative of a switching between upper and lower branches of the amplitude hysteresis loop, which may be accompanied by substantial three-dimensional flow. The range of reduced velocities over which this fluctuation can occur is larger than previously described, and in any event cannot be confined to a single reduced velocity. This transitional regime coincides with the phase change between '2S' and '2P' wake structures, but the lift coefficient total magnitude sees no appreciable change through the switching; lift is most sensitive at $V_{rn} = 4.0$, well inside the '2S' region (*II*). Thus, the free-vibration forcing, as a whole, undergoes a broader change than can be ascertained from any of the phase, lift coefficients, or force correlations alone.

In forced vibrations, only a part of this mechanism seems to be replicated. The correspondence between C_{la} in forced– and free–vibration tests is remarkably close, and indicates that the added mass component of VIV can be parameterized successfully from forced experiments. Similarly, zero power-flow in the forced-oscillations holds on a contour which is fairly close to the free-vibration trajectory, noteworthy because forced vibrations, by definition, cannot *enforce* zero power flow. At the same time, however, the forced vibrations preserve the correlation of end forces somewhat better than the free vibrations. This discrepancy is significant because of the role force correlation must play in extrapolating results from a short test section into a distributed structure with spatially-extended modes.

In the cases considered here, the forced-vibration tests are inadequate to fully

characterize the end forces, and consequently, the spanwise wake. On the other hand, free vibration modes with extended span appear to reinforce long correlation lengths: Brika & Laneville [8], for example, report that anemometer phase angles along their extended beam are virtually uniform, even at the transition from '2S' to '2P' shedding. Hence, although the present data reveals a disagreement between forced and free rigid-cylinder vibrations, this difference might be obviated when distributed structure vibration is considered.

The role of end forces in studying correlation length will be unresolved without visualization studies, although presumably two-dimensional shedding, or shedding with stable cells, leads to a strong correlation between end forces. There are two mechanisms by which the force correlation could be low. The first possibility is that abrupt switching between '2S' and '2P' occurs along the entire length, but the rapid transients prevent the forces from aligning. The second possibility, three-dimensional shedding, appears more likely for several reasons. In the paper, Techet *et al.* [45] and as explained in chapter 4, visualizations employing forced vibrations show that phase-locked '2S' and '2P' modes can coexist on the same test section, in shear conditions. This evidence of a completely stable three-dimensional near wake also points to the possibility of three-dimensional variations in transition, rather than distinct mode changes over the entire span.

Tapered cylinder tests show a reduction in the force correlations for forced–vibration tests, allowing a somewhat better correspondence between forced– and free–vibration tests, than in the uniform case. Thus, the extrapolation from forced to free vibrations is potentially more promising for the case of taper. The extension of these results to shear in the oncoming flow, simulated here with a tapered cylinder, leads to a greater prominence and more gradual decay of the wake transition region during free vibrations. This trend, based on phase angle and force correlation, suggests that the shear provides an effective mechanism for extending the V_{rn} scale above 6.0. Remarkably, the shear also brings about mode synchronization much earlier than in

the uniform case, and in fact, it overlaps with the correlated '2S'-type response. In contrast, for the uniform cylinder, synchronization occurs only in and above Region 3, and has generally been associated with '2P' shedding. The presence of synchronization at all points above $V_{rn} = 3.0$ indicates a wide parametric region over which the structural mode will be excited. Many of the VIV models involving shear, e.g. Vandiver & Chung [49] and Gopalkrishnan *et al.* [17], base their results on an extrapolation of uniform-flow results through distributed structural models. The result that synchronization in shear flow can occur at substantially reduced V_{rn} allows for larger spatial regions of locked-on forcing, altering the predicted response.

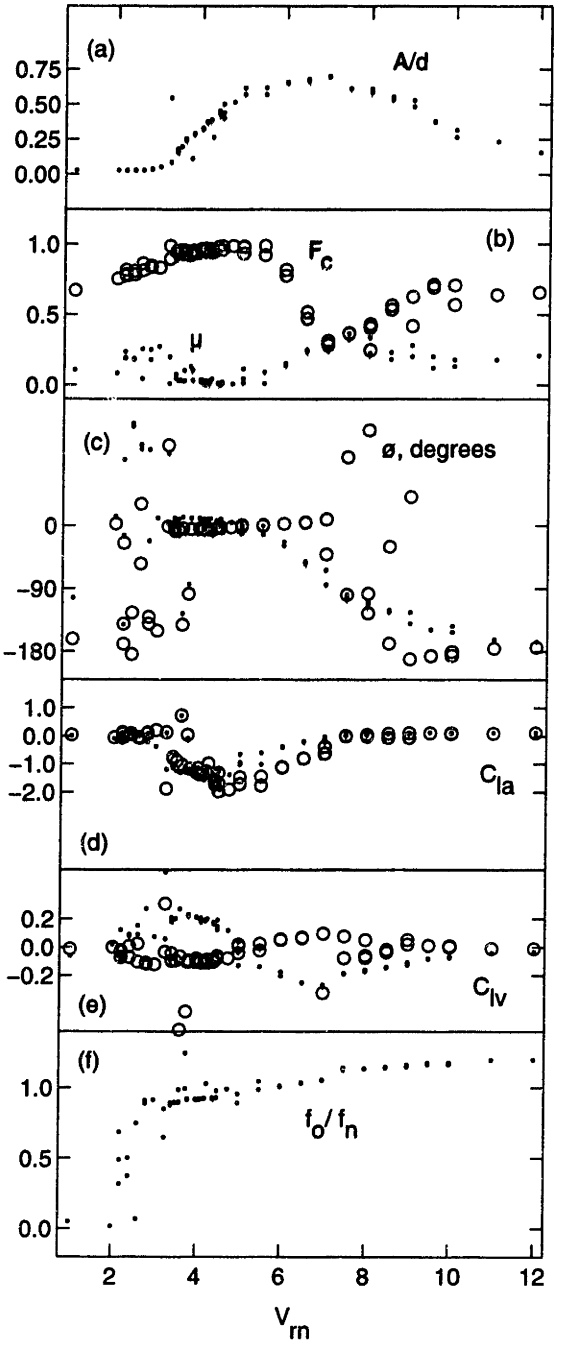

Figure 5-2: The tapered cylinder free response characteristics. For ϕ, C_{la}, and C_{lv}, '.' and 'o' denote the smaller and larger ends of the cylinder, respectively. From Hover et. al. [24]

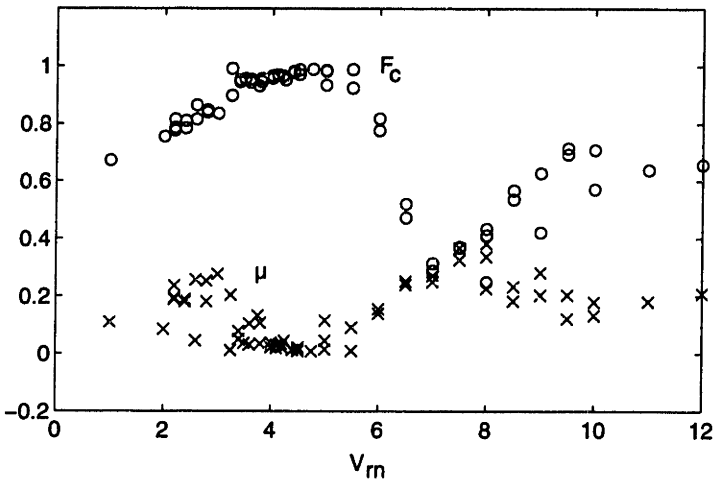

Figure 5-3: Force correlations for the tapered cylinder.

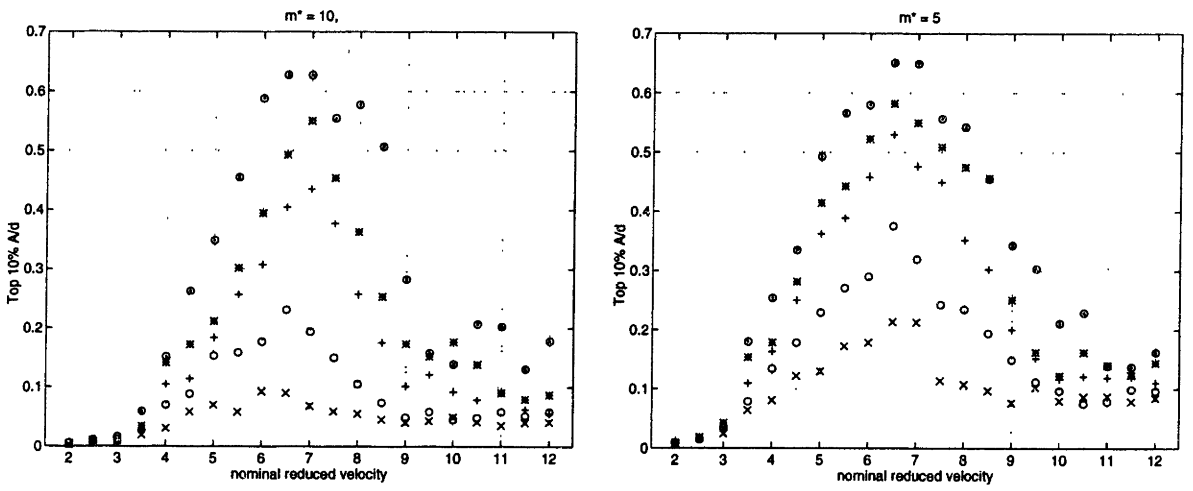

a: $m^* = 10$ b. $m^* = 5$

Figure 5-4: The tapered cylinder free response characteristics. These plots represent the top 10% amplitude to diameter achieved for each reduced velocity and damping parameter: 'x' = 0.1, 'o' = 0.05, '+' = 0.02, '$*$' = 0.01, '.' = 0.00.

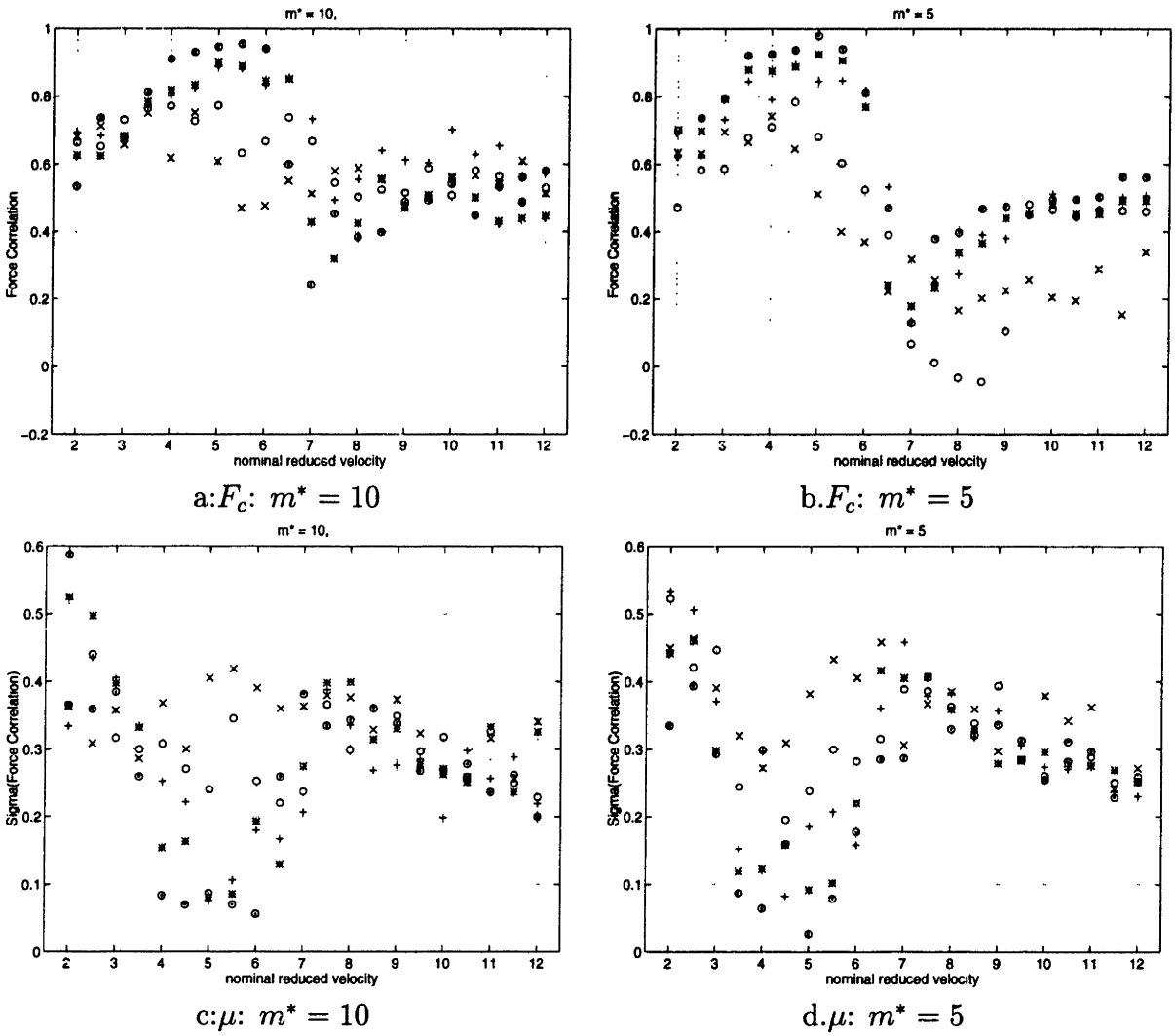

a:F_c: $m^* = 10$

b.F_c: $m^* = 5$

c:μ: $m^* = 10$

d.μ: $m^* = 5$

Figure 5-5: The tapered cylinder free response characteristics. These plots represent the end force correlation (and and standard deviation for each reduced velocity and damping parameter: 'x' = 0.1, 'o' = 0.05, '+' = 0.02, '$*$' = 0.01, '.' = 0.00.

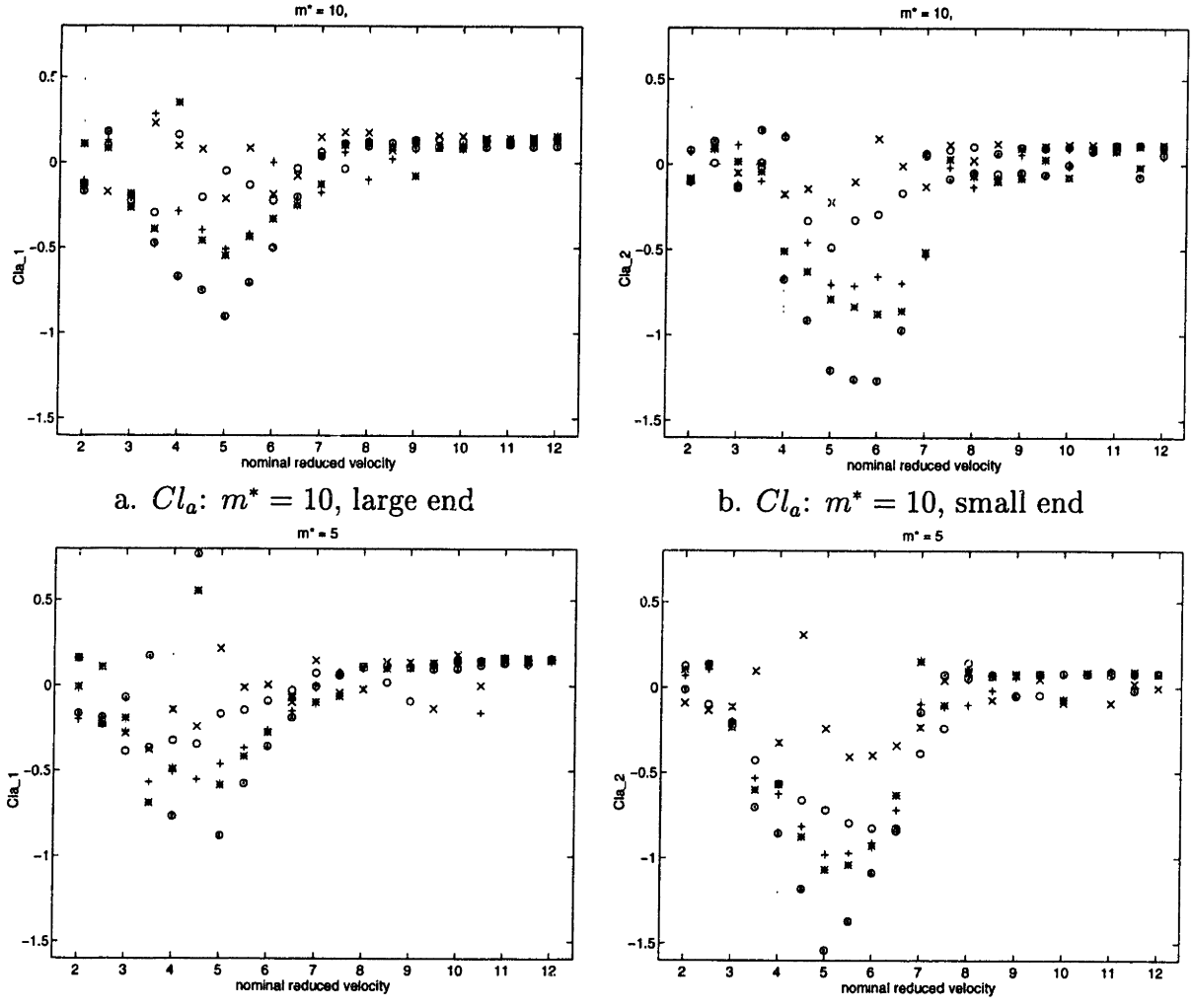

a. Cl_a: $m^* = 10$, large end

b. Cl_a: $m^* = 10$, small end

c. Cl_a: $m^* = 5$, large end

d. Cl_a: $m^* = 5$, small end

Figure 5-6: The tapered cylinder free response characteristics. Figures (a-d) show the lift coefficient in phase with acceleration for five damping parameters: 'x' = 0.1, 'o' = 0.05, '$+$' = 0.02, '$*$' = 0.01, '$.$' = 0.00.

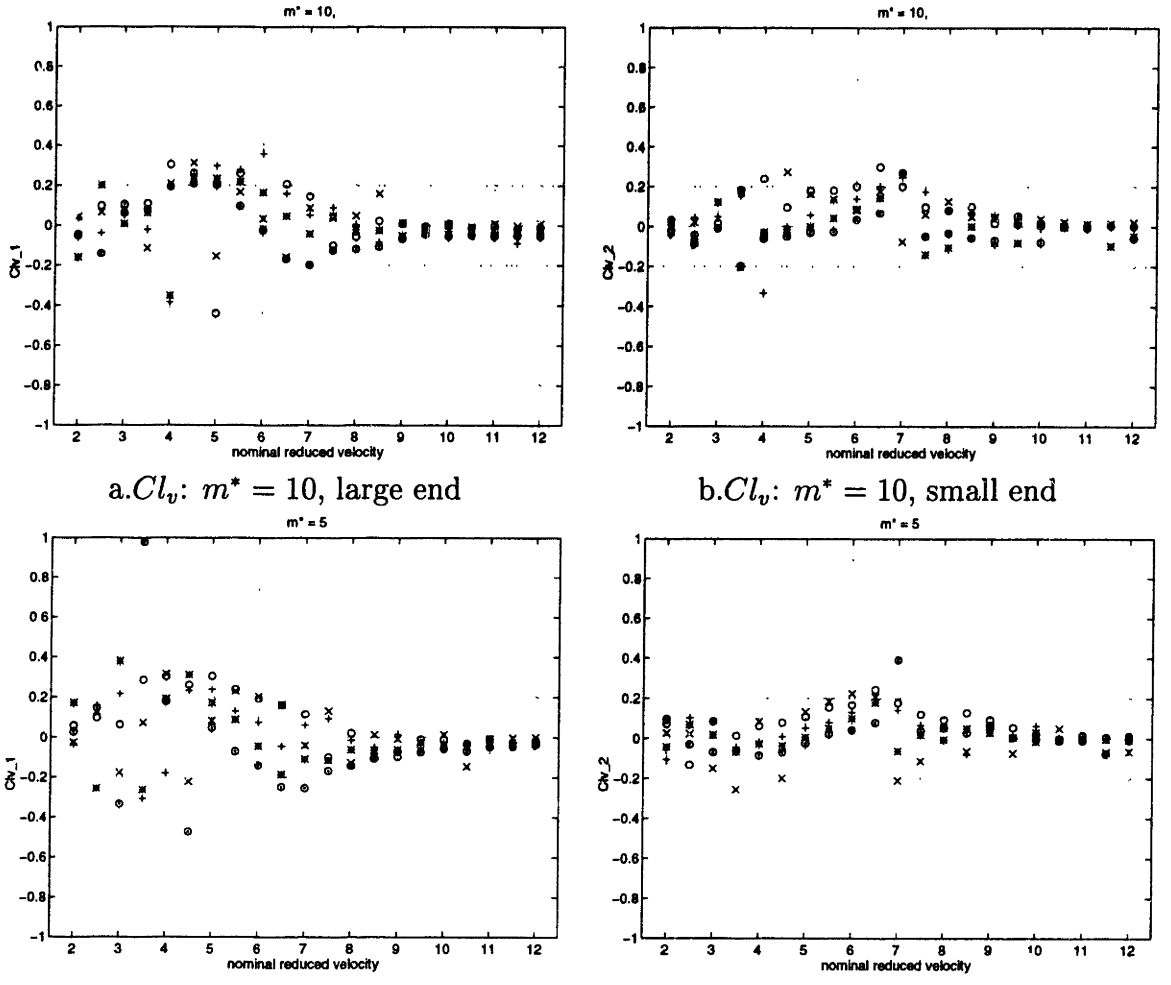

a.Cl_v: $m^* = 10$, large end

b.Cl_v: $m^* = 10$, small end

c.Cl_v: $m^* = 5$, large end

d.Cl_v: $m^* = 5$, small end

Figure 5-7: The tapered cylinder free response characteristics. Figures (a-d) show the lift coefficient in phase with the cylinder velocity for five damping parameters: 'x' = 0.1, 'o' = 0.05, '+' = 0.02, '$*$' = 0.01, '.' = 0.00.

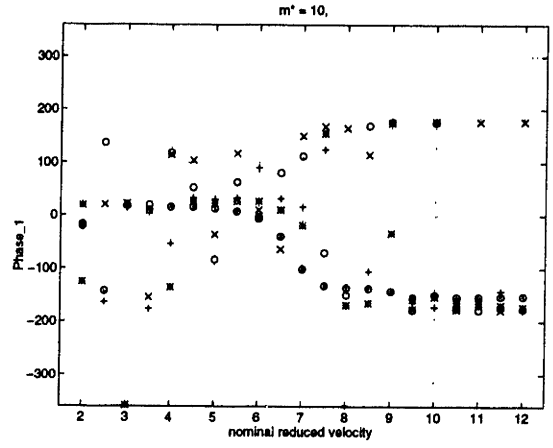

a: ϕ large end: $m^* = 10$

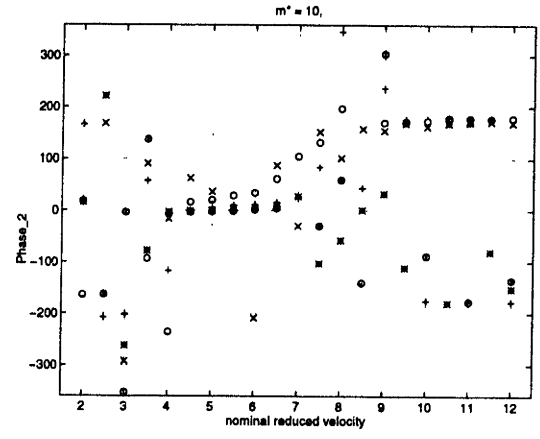

b. ϕ small end: $m^* = 10$

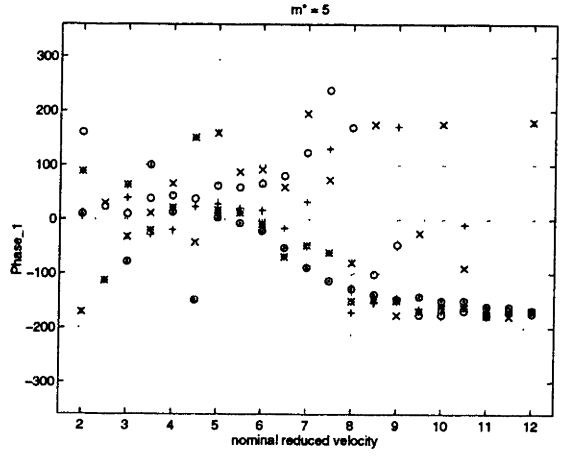

c: ϕ large end: $m^* = 5$

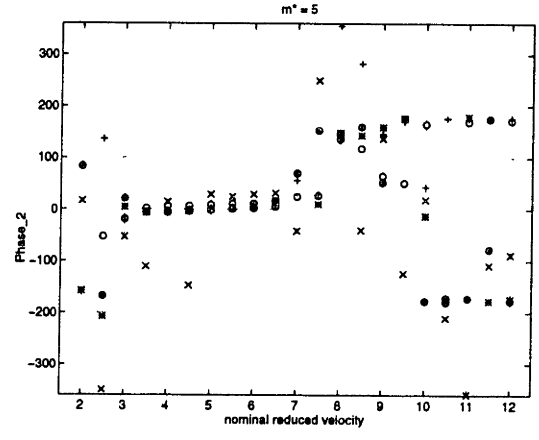

d. ϕ small end: $m^* = 5$

Figure 5-8: The tapered cylinder free response characteristics. These plots represent the phase in degrees for each reduced velocity and damping parameter: 'x' = 0.1, 'o' = 0.05, '+' = 0.02, '$*$' = 0.01, '.' = 0.00.

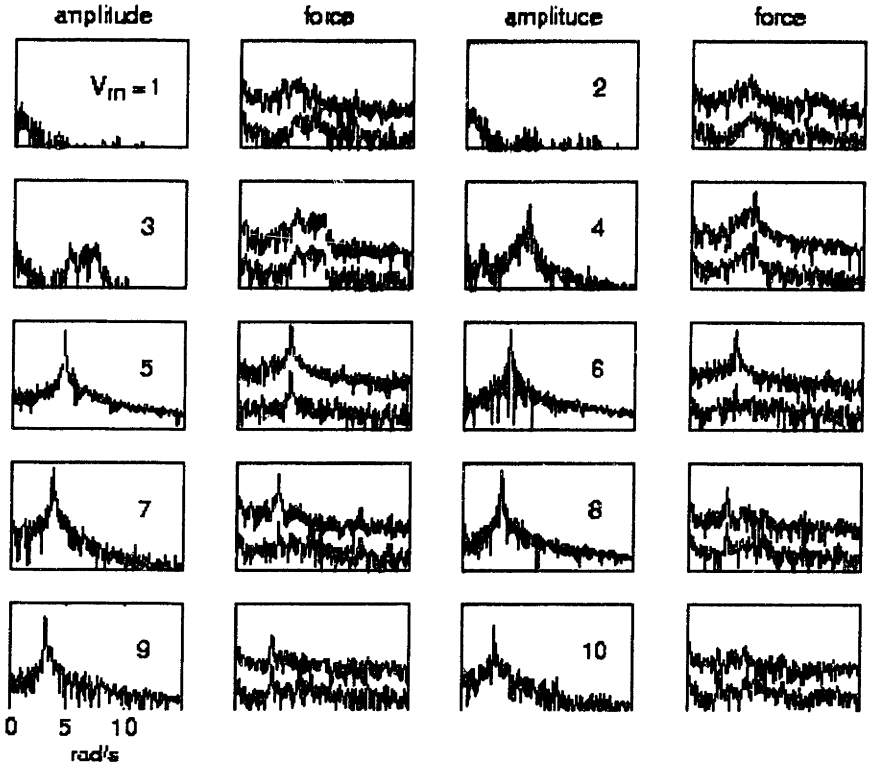

Figure 5-9: Amplitude and force power spectra for the tapered cylinder.

Chapter 6

Concluding Remarks

The topology of vortical pattern formation behind oscillating uniform and tapered cylinders in a uniform stream is a subject of great theoretical and practical interest. The flow around a circular cylinder has become the canonical problem of flow around bluff bodies, presenting very rich dynamic behavior despite its geometric simplicity. Applications are many in diverse systems involving structural and acoustic vibrations. A smoothly tapered cylinder introduces a geometry that is a perturbation from a nominally two–dimensional one, and hence constitutes an important step in assessing systematically the effects of geometric changes and, equivalently, flow shear. Despite efforts spanning several decades, there are still unmapped physical mechanisms of vortex formation even for uniform cylinders, especially for higher Reynolds numbers.

Experimental work can be used to gain insight into the forces, by modeling long cables in sections. Heretofore much work has been done on two-dimensional (spanwise uniform) cylindrical bluff bodies. The focus on tapered oscillating cylinders leads us down another path, into uncharted waters.

This study has uncovered a novel shedding mode present in the 40:1 oscillating tapered cylinder. This hybrid mode is periodic, unlike typical vortex dislocations, and the location of the vortex split remains stable and repeatable, within one to two diameters, depending on the amplitude and frequency of oscillation and the Reynolds

number. The spanwise region of transition from one mode to the other, corresponds nicely with the '2S' to '2P' transition found by Williamson and Roshko (1998). A similar vortex dislocation phenomenon may be found in the case of cylinders with different geometry. For example, the uniform cylinder near lock-in is found to jump from one shedding mode to the next. Whether at any instant the entire cylinder switches or whether the spanwise pattern is hybrid is still unknown. Further investigation is warranted, combining both force measurement and flow-visualizations. Together these techniques can yield powerful information into vortex induced vibrations.

Bibliography

[1] R.J. Adrian. Multi-point optical measurements of simultaneous vectors in unsteady flow—a review. *Int. J. Heat Fluid Flow*, 7:127–145, 1986.

[2] R.J. Adrian. Particle-imaging techniques for experimental fluid mechanics. *Ann. Rev. Fluid Mech.*, 23:261–304, 1991.

[3] E.A. Anderson and A.A. Szewczyk. Vortex shedding from a straight and tapered circular cylinder in uniform and shear flow. *Proc. Sixth International Conf. Flow-Induced Vibrations*, pages 61–71, 1995.

[4] B. Bays-Muchmore and A. Ahmed. On streamwise vortices in turbulent wakes of cylinders. *Physics of Fluids*, A(5):387–392, 1993.

[5] R.E.D. Bishop and A.Y. Hassan. The lift and drag forces on a circular cylinder oscillating in a flowing fluid. *Proc. R. Soc. Lond. A*, 277:51–75, 1964.

[6] R.D. Blevins. *Flow-Induced Vibration.* Van Nostrand Reihnhold Company, New York, NY, 1990.

[7] M.S. Bloor. The transition to turbulence in the wake of a circular cylinder. *J. Fluid Mech.*, 19:290–304, 1964.

[8] D. Brika and A. Laneville. Vortex–induced vibrations of a long flexible circular cylinder. *J. Fluid Mech.*, 250:481–508, 1993.

[9] C. Chyu and D. Rockwell. Evolution of patterns of streamwise vorticity in the turbulent wake of a circular cylinder. *J. Fluid Mech.*, 320:117–137, 1996.

[10] M. Coutanceau and J.R. Defaye. Circular cylinder wake configurations: A flow visualization survey. *Appl. Mech. Rev.*, 44:255–305, 1991.

[11] H. Eisenlohr and H. Eckelmann. Vortex splitting and it consequences in the vortex street wake of cylinders at low reynolds numbers. *Physics of Fluids A*, 1:189–192, 1989.

[12] C.C. Feng. The measurement of vortex–induced effects in flow past stationary and oscillating circular and d–section cylinders. M.a.sc. thesis, University of British Columbia, B.C., Canada, 1968.

[13] M. Gaster. Vortex shedding from slender cones at low reynolds numbers. *J. Fluid Mech.*, 38:565–576, 1969.

[14] M. Gaster. Vortex shedding from circular cylinders at low reynolds numbers. *J. Fluid Mech.*, 46:746–756, 1971.

[15] J.H. Gerrard. The wakes of cylindrical bluff bodies at low reynolds number. *Philos. Trans. R. Soc. London*, 288:351–378, 1978.

[16] R. Gopalkrishnan. *Vortex-induced forces on oscillating bluff cylinders.* PhD thesis, Massachusetts Institute of Technology/Woods Hole Oceanographic Institution, Cambridge, MA, 1992.

[17] R. Gopalkrishnan, M.A. Grosenbaugh, and M.S. Triantafyllou. Amplitude modulated cylinders in constant flow: Fundamental experiments to predict response in shear flow. *Proc. Third Int. Symp. on Flow-Induced Vibrations and Noise, ASME*, 1992.

[18] J.M.R. Graham and R.H. Arkell. The effects of waves on vortex shedding from cylinders. In *Bluff-body wakes, dynamics and instabilities*, pages 19–22, Gottingen; Germany, September 1992. International Union of Theoretical and Applied Mechanics., Springer-Verlag.

[19] O.E. Griffin. Flow near self-excited and forced vibrating circular cylinders. *J. Eng. Industry*, pages 539–547, May 1972.

[20] P. Yang H. Mansy and D. Williams. Quantitative measurements od three-dimensional structures in the wake of a circular cylinder. *J. Fluid Mech.*, 270:277–296, 1994.

[21] M. Hammache and M. Gharib. An experimental study of the parallel and oblique vortex shedding from circular cylinders. *J. Fluid Mech.*, 232:567–590, 1991.

[22] H. Honji, S. Taneda, and M. Tatsuno. Some practical details of the electrolytic precipitation method of flow visualization. *Reports of Research Inst. for Appl. Math.*, 28:83–89, 1980.

[23] F.S. Hover, S.N. Miller, and M.S. Triantafyllou. Vortex-induced vibration of marine cables: Experiments using force feedback. *J. Fluids Struct.*, 11:306–326, 1997.

[24] F.S. Hover, A.H. Techet, and M. S. Triantafyllou. Forces on oscillation uniform and tapered cyinders in crossflow. *J. Fluid Mech.*, 1998 (to appear).

[25] J.A. Humphries. *Vortex induced vibrations in sheared flow.* PhD thesis, Cranfield Institute of Technology, 1987.

[26] G.E. Karniadakis and G.S. Triantafyllou. Three-dimensional dynamics and transition to turbulence in the wake of bluff objects. *J. Fluid Mech.*, 238:1–30, 1992.

[27] A. Khalak and C.H.K Williamson. Dynamics of a hydroelastic cylinder with very low mass and damping. *J. Fluids Struct.*, 10:455–472, 1996.

[28] M. Konig, H. Eisenlohr, and H. Eckelmann. Visualization of the cellular structure of the laminar wake of wall-bounded circular cylinders. *Phys. Fluids A*, 4:869–872, 1991.

[29] C.G. Lewis and M. Gharib. An exploration os the wake of three dimensionalities caused by a local discontinuity in cylinder diameter. *Phys. Fluids A*, 4(1):104–117, 1992.

[30] J.C. Lin, P. Vorobieff, and D. Rockwell. Space–time imaging of a turbulent near–wake by high–image–density particle image cinematography. *Physics of Fluids*, 8(2):555–564, 1996.

[31] M. Nakano and D. Rockwell. Flow structure in the frequency–modulated wake of a cylinder. *J. Fluid Mech.*, 266:93–19, 1994.

[32] E. Naudascher and D. Rockwell. *Flow-Induced Vibrations.* A.A. Balkema, Rotterdam, 1994.

[33] D. Newman and G.E. Karniadakis. Simulations of flow over a flexible cable: A comparison of forced and flow–induced vibration. *J. Fluids Struct.*, 10:439–453, 1996.

[34] A. Papangelou. Vortex shedding from slender cones at low reynolds numbers. *J. Fluid Mech.*, 242:299–321, 1992.

[35] G. Parkinson. Phenomena and modelling of flow-induced vibrations of bluff bodies. *Prog. Aerospace Sci.*, 26:169–224, 1989.

[36] P.S. Piccirillo and van Atta. An experimental study of vortex shedding behind linearly tapered cylinders at low reynolds number. *J. Fluid Mech.*, 246:163–195, 1993.

[37] S.E. Ramberg and O. Griffin. Velocity correlation and vortex spacing in the wake of a vibrating cables. *J. Fluids Engineering*, pages 10–18, 1976.

[38] A. Roshko. On the development of turbulent wakes from vortex streets. *NACA Report*, 1191:1–23, 1954.

[39] T. Sarpkaya. Transverse oscillations of a circular cylinder in uniform flow. Technical Report NPS-69SL77071, Naval Postgraduate School, Monterey, Monterey, California, 1977.

[40] T. Sarpkaya. Hydrodynamic damping, flow-induced oscillations, and biharmonic response. *J. Offshore Mech. Arctic Eng.*, 117:232–238, 1995.

[41] A. Slaouti and J.H. Gerrard. An experimental investigation of the end effects on the wake of a circular cylinder towed through water at low reynolds numbers. *J. Fluid Mech.*, 112:297–314, 1981.

[42] P.K. Stansby. The locking-on of vortex shedding due to the cross-stream vibration of circular cylinders in uniform and shear flows. *J. Fluid Mech.*, 74:641–655, 1976.

[43] T. Staubli. Calculation of the vibration of an elastically mounted cylinder using experimental data from forced oscillation. *J. Fluids Eng.*, 105:225–229, 1983.

[44] S. Szepessy. On the spanwise correlation of vortex shedding from a circular cylinder at high subcritical reynolds number. *Physics of Fluids*, 6:2406–2416, 1994.

[45] A.H. Techet, F.S. Hover, and M. S. Triantafyllou. Vortical patterns in the wake of a tapered cylinder oscillating transversely to a uniform flow. *J. Fluid Mech.*, 1998 (to appear).

[46] J. Towfighi and D. Rockwell. Flow structure from an oscillating nonuniform cylinder: Generation of patterned vorticity concentrations. *Physics of Fluids*, 6:531–536, 1994.

[47] G.S. Triantafyllou. Three–dimensional flow patterns in two dimensional wakes. *J. Fluids Eng.*, 114:356–361, 1992.

[48] M.S. Triantafyllou. Vortex-induced vibrations of cables and hawsers in water. In *Invited Review Lecture on Fluid-Structure Interaction International Symposium on Cable Dynamics*, Liege, Belgium, October 1995.

[49] J.K. Vandiver and T.Y. Chung. Hydrodynamic damping on flexible cylinders in sheared flow. *Proc. OTC*, pages 343–353, 1987.

[50] T. Wei and C.R. Smith. Secondary vortices in the wake of circular cylinders. *J. Fluid Mech.*, 169:513–533, 1986.

[51] C. E. Willert and M. Gharib. Digital particle image velocimetry. *Exps. Fluids*, 10:181–193, 1991.

[52] C.H.K. Williamson. The natural and forced formation of spot–like 'vortex dislocations' in the transition of a wake. *J. Fluid Mech.*, 243:393–441, 1992.

[53] C.H.K. Williamson. Three-dimensional wake transition. *J. Fluid Mech.*, 328:345–407, 1996.

[54] C.H.K. Williamson. Vortex dynamics in the wake. *Annual Rev. Fluid Mech.*, 28:477–539, 1996.

[55] C.H.K. Williamson and A. Roshko. Vortex formation in the wake of an oscillating cylinder. *J. Fluids and Structures*, 2:355–381, 1988.

[56] J. Wu, J. Sheridan, M.C. Welsh, and K. Houridan. Three-dimensional vortex structures in a cylinder wake. *J. Fluid Mech.*, 312:201–222, 1996.

[57] J. Wu, J. Sheridan, M.C. Welsh, K. Houridan, and M. Thompson. Longitudinal vortex structures in a cylinder wake. *Physics of Fluids*, 6(9):2885–2885, 1994.

[58] P.M. Yang, H. Mansy, and D.R. Williams. Oblique and parallel wave interaction in the near wake of a circular cylinder. *Phys. Fluids A*, 5:1657–1660, 1994.

[59] H.Q. Zhang, U. Fey, B.R. Noack, M. Konig, and H. Eckelmann. On the transition of the cylinder wake. *Physics of Fluids*, 7:779–794, 1995.

[60] Y. Zhou and A. Antonia. Critical points in a turbulent near wake. *J. Fluid Mech.*, 275:59–81, 1994.

THESIS PROCESSING SLIP

FIXED FIELD: ill. _____ name _____

index _____ biblio _____

▶ COPIES: (Archives) Aero Dewey (Eng) Hum
Lindgren Music Rotch Science

TITLE VARIES: ▶☐ _____

NAME VARIES: ▶☐ _____

IMPRINT: (COPYRIGHT) _____

▶ COLLATION: AAV 92 P

▶ ADD: DEGREE: _____ ▶ DEPT.: _____

SUPERVISORS: _____

NOTES:

cat'r: date:

page: 100

▶ DEPT: C.E.

▶ YEAR: 1998 ▶ DEGREE: S.M.

▶ NAME: TECHET, Alexandra Hughes